

Spectroscopic studies of atomic defects and bandgap renormalization in semiconducting monolayer transition metal dichalcogenides

Tae Young Jeong^{1,2*}, Hakseong Kim^{1*}, Sang-Jun Choi³, Kenji Watanabe⁴, Takashi Taniguchi⁴,
Ki Ju Yee², Yong-Sung Kim^{1§} and Suyong Jung^{1§}

¹Quantum Technology Institute, Korea Research Institute of Standards and Science, Daejeon
34113, Korea

²Department of Physics, Chungnam National University, Daejeon 34134, Korea

³Center for Theoretical Physics of Complex Systems, Institute for Basic Science, Daejeon 34126,
Korea

⁴Advanced Materials Laboratory, National Institute for Materials Science, 1-1 Namiki, Tsukuba
305-0044, Japan

Abstract

Assessing atomic defect states and their ramifications on the electronic properties of two-dimensional van der Waals semiconducting transition metal dichalcogenides (SC-TMDs) is the primary task to expedite multi-disciplinary efforts in the promotion of next-generation electrical and optical device applications utilizing these low-dimensional materials. Here, with electron tunneling and optical spectroscopy measurements with density functional theory, we spectroscopically locate the mid-gap states from chalcogen-atom vacancies in four representative monolayer SC-TMDs—WS₂, MoS₂, WSe₂, and MoSe₂—, and carefully analyze the similarities and dissimilarities of the atomic defects in four distinctive materials regarding the physical origins

* These authors contributed equally to this work.

§ To whom correspondence should be addressed yongsung.kim@kriss.re.kr or syjung@kriss.re.kr

of the missing chalcogen atoms and the implications to SC-mTMD properties. In addition, we address both quasiparticle and optical energy gaps of the SC-mTMD films and find out many-body interactions significantly enlarge the quasiparticle energy gaps and excitonic binding energies, when the semiconducting monolayers are encapsulated by non-interacting hexagonal boron nitride layers.

Introduction

Atomic defect states in two-dimensional semiconducting transition metal dichalcogenides (SC-TMDs) are credited to many intriguing scientific and engineering aspects such as single quantum emitters,¹⁻⁴ single-atom magnetism,⁵ and defect-modulating dopings,^{6,7} to name a few. Defect states have the implications to decide the specific type of SC-TMD, while defect-related trap states adjust the position of the Fermi level (E_F) with respect to conduction and valence bands.⁶⁻⁹ The presence of atomic defects along with charged impurities is also known to limit charged carrier mobilities and induce a strong Fermi-level pinning at the metal/SC-TMD interfaces, thereby limiting SC-TMD-based electronic applications.¹⁰ Thus, examining the origins and spectral locations of defect-induced states is prerequisite to the full utilization of such states in SC-TMDs and the building-up of TMD-based device functionalities. Experimental analyses of such defects typically rely on imaging methods like transmission electron microscopy (TEM) and scanning tunneling microscope (STM), visualizing the various forms of atomic defects in SC-TMDs.^{6,7,10-13} Although some STM studies have provided experimental signatures of the mid-gap states from atomic defects in SC-TMDs,¹⁴ the majority of outstanding questions, such as those concerning the defect-induced mid-gap states and their spectral locations inside the energy gaps, have mostly relied on theoretical predictions.⁸

We note that spectroscopic investigations of defect-induced mid-gap states should be accompanied by the identification of other key SC-mTMD material parameters; the quasiparticle energy gaps (E_g) and the position of E_F inside the gaps. For example, chalcogen-atom vacancies (V_S, V_{Se}), the most common defects in S- and Se-based SC-TMDs, are expected to induce mid-gap states: singlet a_1 states forming close to the valence band and doublet e states forming deep inside the energy gap.^{6,8} Quite surprisingly, however, experiment and theory have yet to agree on the most fundamental SC-mTMD property, the quasiparticle energy gaps. For example, such energy gaps inferred from different experiments have varied up to ≈ 1 eV,¹⁵ and theoretically expected energy-gap sizes also differ depending on the extent of Coulombic interactions.^{15,16} Accordingly, excitonic binding energies (E_B), or the energy difference between quasiparticle and optical energy gaps (E_{opt}), are reported to vary from a few hundredth of meV to ≈ 1 eV.¹⁷⁻²¹

In this article, we carry out careful electron tunneling, optical spectroscopy measurements, and density functional theory (DFT) calculations for four representative SC-mTMDs—mWS₂, mMoS₂, mWSe₂, and mMoSe₂—to accurately assess material parameters such as the mid-gap states from chalcogen atom vacancies, the quasiparticle energy gaps and exciton binding energies, and other material specifications. We are able to identify the mid-gap states from chalcogen-atom vacancies in the SC-mTMDs by introducing *h*-BN as a tunnel barrier and graphene as a spectrum analyzer in van der Waals (vdW)-based planar heterostructures. Defect-induced mid-gap states in the four respective films reveal similarities and dissimilarities regarding the spectral locations of the defect states, mechanisms of vacancy formation, and overall defect density of states (DOS). Our studies suggest that single-atom defects in SC-mTMDs present direct experimental implications that chalcogen-atom vacancies turn into active charged dopants. Moreover, we can accurately determine the quasiparticle energy gaps and exciton binding energies of the four SC-

mTMDs via electron tunneling, optical reflectance/transmission spectroscopy, and temperature-dependent photoluminescence (PL) measurements. We confirm that the electronic structures of the SC-mTMDs are greatly renormalized by electron–electron interactions. With temperature-dependent PL, we then assess the excitonic binding energies of these monolayers to be as large as ≥ 0.78 eV, when the films are encapsulated by *h*-BN and graphene.

Results

2D vdW planar tunnel junctions with SC-mTMDs. An optical viewgraph and schematic of the vdW heterostructure for probing the electronic and optical properties of SC-mTMDs are displayed in Figure 1a. Here, we list a few experimental highlights for implementing graphene as the bottom contact to a given SC-mTMD. First, direct metal contact to a SC-mTMD induces electronic and physical deformations on the film, which renders contact resistances comparable to or even larger than tunnel resistances through the *h*-BN barriers at low temperatures. This additional resistance along the path of tunnel electrons violates the ultimate priori for electronic tunneling spectroscopies, requiring that a major voltage drop occur at the tunnel junction in order for sample-bias voltage (V_b) to be associated with tunnel-electron energy with respect to the Fermi level (E_F). Thus, a reliable and low-resistance metal–SC-mTMD contact, which we have achieved via the bottom graphene, is critical for accurately addressing the electronic structures of SC-mTMDs.

The second advantageous role of the graphene bottom contact is that it allows the single-atom carbon layer to be used as a spectrum analyzer. As schematically illustrated in Figure 1b, tunnel electrons injected from the graphite probe detect the electronic band structure of the SC-mTMD only if the tunnel electrons possess higher (lower) energies than the conduction (valence) band of the SC-mTMD. Otherwise, tunnel electrons exclusively detect the bottom graphene

through the energy-gap windows of both *h*-BN and SC-mTMD. Thus, any deviations in the spectra from the graphite–insulators–graphene tunnel junction, noted hereafter as the graphene baseline, should be attributed to the electronic structure of the SC-mTMD and the probable mid-gap states. The third role of the graphene is to minimize probe-induced charging effects. During tunneling measurements, the effective electric field between the probe and SC-mTMDs through the *h*-BN barrier becomes strong when V_b increases up to $|V_b| \geq 1$ V. Thus, probe-induced charges and consequent electronic structure modifications in the SC-mTMD could cause serious complications in accurately analyzing tunnel spectra.^{22,23} Thanks to a much larger charge compressibility of the graphene, however, induced charges accumulate only on the bottom graphene when V_b is within the energy gaps, thereby allowing us to probe the intrinsic band structure of the SC-mTMD.

Electron tunneling and optical spectroscopy measurements. Figure 1d shows a collection of tunneling spectra, differential conductance ($G = dI/dV_b$) curves as a function of V_b from mWS₂, mMoS₂, mWSe₂, and mMoSe₂ planar junctions at $T \leq 4$ K. In our scheme, V_b is applied to a graphite probe with the SC-mTMD–graphene connected to a current preamplifier. Thus, negative (positive) V_b corresponds to the empty (filled) states of the SC-mTMD at a positive (negative) energy with respect to E_F . The colored arrows in Figure 1d respectively represent the locations of the quasiparticle energy gaps of the SC-mTMDs; detailed methods for locating the energy gaps will be described in later sections. The inset in Figure 1d displays a graphene baseline dI/dV_b with the Dirac point of graphene tuned at $V_b = 0$ V, and green lines indicate numerical fittings to experimental data (red circles).^{22,24} We compare several graphite–*h*-BN–graphene junctions and find out that all tunnel spectra maintain similar dI/dV_b characteristics

only differentiated by multiplication constants, predetermined by the tunnel *h*-BN thicknesses and junction areas (Supplementary Figure 1).

Our planar heterojunctions allow us to address both electronic and optical SC-mTMD properties without switching device platforms. Figure 1e shows a collection of PL measurements at $T = 300$ K and $T = 80$ K from identical SC-mTMD-based planar devices. The dominant PL peak, identified as an *A* exciton that determines the optical energy gap of the particular SC-mTMD, is measured right at the tunnel junction where the monolayers are encapsulated by thin *h*-BN and graphite probe on top, and graphene and thick *h*-BN on the bottom (Supplementary Figure 2). As previously reported^{25,26} and confirmed from our devices, *A*-exciton peaks of SC-mTMDs blue-shift as temperature decreases in the range of $80 \text{ K} \leq T \leq 300 \text{ K}$. Following the Varshni relation,²⁵ we extrapolate the *A*-exciton peak at $T = 0$ K and assign it as the E_{opt} of the SC-mTMD encapsulated with graphene and *h*-BN, such as $E_{\text{opt}}(\text{mWS}_2) = 2.051 \text{ eV}$, $E_{\text{opt}}(\text{mMoS}_2) = 1.936 \text{ eV}$, $E_{\text{opt}}(\text{mWSe}_2) = 1.724 \text{ eV}$, and $E_{\text{opt}}(\text{mMoSe}_2) = 1.638 \text{ eV}$ (Supplementary Figures 3 and 4).

We can independently measure the spin-orbit coupling (SOC)-induced valence-band splittings by locating the *A* and *B* excitonic peaks through optical reflectance and transmittance measurements (Supplementary Figure 5). The inset in Figure 1e shows reflectance spectra from the mWS₂ device at $T = 80$ K and $T = 300$ K. Both excitonic peaks are clearly identifiable, as well as *A*–*B* exciton spacing; therefore, the SOC-induced valence-band splitting (Δ_{SO}) is determined to be $\Delta_{\text{SO}}(\text{mWS}_2) \approx 0.38 \text{ eV}$. Note that Δ_{SO} is weakly dependent on temperature unlike the individual peak positions of *A* and *B* excitons, and Δ_{SO} is less susceptible to the dielectric environments. We prepare several SC-mTMDs on different substrates and find that the *A*–*B* exciton spacings are consistent, within an uncertainty level of $\pm 0.01 \text{ eV}$, with varying dielectric environments and temperatures (Supplementary Table 1). With optical measurements, therefore, we can determine

the SOC-induced valence-band splittings of all four SC-mTMDs: $\Delta_{\text{SO}}(\text{mWS}_2) = 0.38 \text{ eV}$, $\Delta_{\text{SO}}(\text{mMoS}_2) = 0.15 \text{ eV}$, $\Delta_{\text{SO}}(\text{mWSe}_2) = 0.43 \text{ eV}$, and $\Delta_{\text{SO}}(\text{mMoSe}_2) = 0.20 \text{ eV}$ (Supplementary Figure 6).

Assessing atomic defects of S-based SC-mTMDs. Figures 2a and 2c display tunneling spectra from mWS₂ and mMoS₂ devices, replotting dI/dV_b (Figure 1d) in log scale. As displayed in Figure 2a, spectral features at higher V_b are better identified with normalized conductance $(dI/dV_b)/(IV_b)$ plots. To better distinguish dI/dV_b at lower V_b , we numerically average out the original data (light grey lines) and plot the leveled signals (overlaid red lines). Note that signals where V_b is inside the mWS₂ energy gap ($|V_b| \leq 1 \text{ V}$) reveal distinct dI/dV_b variations with more than three orders of magnitude, and these spectra reflect the graphene baseline with both *h*-BN and SC-mTMD as tunnel insulators. Interestingly enough, the graphene baseline and the mWS₂ tunnel signals become well aligned in a V_b range of $|V_b| < 0.7 \text{ V}$ for both filled ($V_b > 0 \text{ V}$) and empty ($V_b < 0 \text{ V}$) states. After a slight dI/dV_b hike at $V_b \approx 0.7 \text{ V}$, the mWS₂ spectra follow the graphite–graphene junction characteristics up to $V_b < 1.5 \text{ V}$ with a minor adjustment at the tunneling constant (dotted green line).

As discussed previously, any deviations from the graphene baseline can be directly related to the SC-mTMD film and its electronic structure. At first, we assign the dI/dV_b peaks at -2.33 eV and -2.21 eV to the valence-band edges of the K and Γ points of the mWS₂, respectively. In mWS₂, the valence-band edge at Γ is expected to be higher in energy than the lower edge of the SOC-split valence band at K. Directly inferred from the optically determined $\Delta_{\text{SO}}(\text{mWS}_2) = 0.38 \text{ eV}$, the higher SOC-split valence band, thus the valence-band edge of mWS₂, should be positioned at -1.95 eV , where we locate a distinct dI/dV_b tunnel feature (Supplementary Figure 7). Following

the same approach, the conduction-band edge at K is assigned at 0.93 eV, and the dI/dV_b peak at 1.05 eV as the conduction-band edge at the Q point. Accounting for all these assignments, the mWS₂ film encapsulated with non-perturbing high-quality *h*-BN and graphene is confirmed to be a direct band-gap *n*-type semiconductor, whose conduction band is closer to E_F than the valence band edge, and with a quasiparticle energy gap $E_g = 2.88$ eV, excitonic binding energy $E_B = 0.83$ eV, and an optical energy gap $E_{opt} = 2.051$ eV. The uncertainty for each energy-level assignment is less than ± 0.01 eV. Complete energy-level alignments for mWS₂ are summarized in the diagram in Figure 2b. We point out that the measured quasiparticle energy gap of mWS₂ is in perfect agreement with theoretical expectations from the GW approach considering many-body perturbation effects.

We now address the mMoS₂ electronic band structures following the above-discussed spectra-analyzing protocol with graphene baseline. As displayed in Figure 2c, the graphene baseline follows most of the dI/dV_b features from the mMoS₂ device in the filled states at $V_b < 1.5$ V. It is intriguing to note that, identical to mWS₂, a slight dI/dV_b increase in value is also present at $V_b \approx 0.7$ V in mMoS₂. Our measurements indicate that the valence band edge at Γ is in alignment with the lower SOC-split band edge at the K point at -2.01 eV, and the dI/dV_b feature at -1.86 eV where the tunnel spectra in log scale evidently changes its slope is assigned as the higher SOC-split valence-band edge at K (Supplementary Figure 7). The valence-band splitting at K is in perfect agreement with optically confirmed $\Delta_{SO}(\text{mMoS}_2) = 0.15$ eV.

Analyzing the mMoS₂ dI/dV_b in the empty states, however, is not as straightforward as for mWS₂ or the filled states of mMoS₂. At first, dI/dV_b in the empty states are significantly larger than the values in the filled states, by more than two orders of magnitude, making mMoS₂ dI/dV_b highly asymmetric around E_F . Interestingly though, dI/dV_b becomes realigned with the graphene

baseline at $V_b \approx -0.8$ V with a significantly enhanced dI/dV_b multiplication constant. With that, we assign the conduction band edge of the mMoS₂ at the K point at 0.86 eV, and the dI/dV_b peak at 1.01 eV as the band edge at Q. As a result, mMoS₂ can be considered as a direct band-gap *n*-type semiconductor, with a quasiparticle energy gap $E_g = 2.72$ eV and excitonic binding energy $E_B = 0.78$ eV ($E_{opt} = 1.936$ eV). Again, the experimentally assessed quasiparticle energy gap of the mMoS₂ is in excellent agreement with the predicted energy gaps from GW calculations.^{15,27}

We relate the enormously amplified dI/dV_b in the empty states to the doublet *e* defect states from sulfur-atom vacancies in the mMoS₂. Based on our DFT calculations, the majority of singlet a_1 states in mWS₂ are formed at lower energies than the valence-band edge, concealing most of the defect states under the valence band (see below). The bulk portion of a_1 states in mMoS₂, however, are expected to form at higher energies than the valence-band edge, expecting rather pronounced a_1 -related mid-gap states. Defect states relating to the doublet *e* states are formed deep inside the energy gaps with the mid-gap states in mMoS₂ closer to E_F in the empty states. Our measurements confirm these theoretically expected spectral locations of a_1 and *e* defect states in S-based SC-mTMDs. We specify that the dI/dV_b regions, positioned higher in energy than the valence-band edges, therefore within the energy gaps with dI/dV_b straying from the graphene baseline (depicted in purple in Figures 2a and 2c), reflect the a_1 defect states. It is obvious that the a_1 states in mMoS₂ extend further into the gap when compared with the smaller dI/dV_b region for the mid-gap states in mWS₂. In addition, an evident dI/dV_b hump inside the energy gap of mWS₂, as marked with a red arrow and delineated in orange in Figure 2a, is assigned to the *e* defect states, and their spectral locations are consistent with theoretical calculations (see below). We further note that the defect related dI/dV_b features are not sensitive to external V_g , unlike to spectra relating to underlying graphene and its energy-band alignment with a graphite probe (Supplementary

Figure 8). As compared with the well-isolated e states in mWS₂, however, the mid-gap states in mMoS₂ extend much wider inside the energy gap, making the defect-related tunnel spectra more conspicuous. The enlarged dI/dV_b in the empty state suggests that mMoS₂ films are inclined to contain more sulfur vacancies than mWS₂, and that some of the vacancies are mobile enough to agglomerate into energetically stable line-type defects, as theoretically expected¹³ and experimentally confirmed with TEM analyses.²⁸ In an earlier STM and our theoretical calculations confirm that defect states of neutral disulfur vacancies ($V_S V_S$), the simplest form of vacancy chains in mMoS₂, have $e-e$ divacancy hybridized defect states that are extensively expanded inside the energy gap.²⁹

Assessing atomic defects of Se-based SC-mTMDs. Figures 3a and 3c respectively display the dI/dV_b from mWSe₂ and mMoSe₂ planar devices. Note that tunnel dI/dV_b structures in mWSe₂ are notably lacking around the valence band, and the peak at -2.05 eV and the location where tunnel spectra start deviating from the graphene baseline are quite distant considering the SOC-split valence-band edges, $\Delta_{SO}(\text{WSe}_2) = 0.43$ eV. We attribute these smooth dI/dV_b evolutions to an augmented momentum mismatch of the tunneling electrons from the graphite probe to the mWSe₂ film in this particular tunnel junction. As discussed in previous reports, tunneling spectra from vdW planar heterojunctions are not only sensitive to the sample DOS at a given energy but also rely on the crystal momentum alignments of the tunnel probe (graphite) and the 2D layers of interest (SC-mTMD).³⁰⁻³³ When electrons with momentum \mathbf{k}_{gp} are injected from the graphite probe to the available states of the SC-mTMD at \mathbf{k}_{mTMD} , momentum of the tunnel electrons relaxes by $\Delta k_{||} = |\mathbf{k}_{mTMD} - \mathbf{k}_{gp}|$, which is then directly linked to the probability of electron tunneling. The absolute value of tunnel dI/dV_b is determined by the tunneling decay constant $T \approx (2m_e \Phi_b \hbar^{-2} +$

$(\Delta k_{\parallel})^2)^{1/2}$, where Φ_b is the tunnel barrier and m_e is the effective mass of tunnel electrons. Thus, a larger momentum mismatch (Δk_{\parallel}) of tunnel electrons results in weaker signals and a smaller dI/dV_b in value. Graphite is naturally considered as the most effective tunneling probe for investigating the electronic structures of graphene and SC-mTMDs since most of the interesting features of 2D hexagonal lattice materials are confined to the electronic structures around the K point, at which the Fermi level of the graphite probe is precisely located.³⁴ Here, we need to assert that only parts of the Brillouin zones (BZ) of the graphite probe and SC-mTMDs become matched, even for perfectly aligned planar junctions, because of the lattice mismatch between graphene and SC-TMDs (Supplementary Figure 9). However, electron tunneling through 2D vdW heterojunctions consisting of layered materials with different lattice constants needs to consider extended BZs of the heterostructures and their varying equipotential surfaces depending on V_b . We find that both of which are sensitive to the misalignment angle of the junctions, and tunneling probability becomes highest for perfectly aligned heterostructures, which will be discussed in detail in coming literature.

We fabricate a second type of mWSe₂ tunnel device with crystalline angles of top graphite and mWSe₂ layers tightly aligned in order to efficiently probe the electronic structures around K. As expected, dI/dV_b around the valence-band edge becomes enhanced in value in the tightly aligned device (solid orange line in Figure 3a). Resonant tunnel features with negative dI/dV_b (green circles in Figure 3a) confirm that the crystalline angles of the graphite and mWSe₂ are closely matched.^{30–33} By comparing the dI/dV_b from aligned and misaligned devices, we assign the upper edge of the SOC-split valence bands at -1.21 eV, and the lower SOC-split band edge to a dI/dV_b crest at -1.64 eV, guided by optically determined Δ_{SO} (mWSe₂) = 0.43 eV. The dI/dV_b peak at -2.05 eV is subsequently designated as the valence-band maximum at Γ .

It is interesting to note that tunnel signals from the tightly aligned device in the vicinity of the conduction-band edge differ from the amplified dI/dV_b around the valence band: dI/dV_b at ≈ 1.35 eV are not amplified as much as those around the valence-band maximum at K. Instead, a couple dI/dV_b peaks become conspicuous at 1.50 eV and 1.53 eV in the tightly aligned sample, leading us to assign them as the SOC-split conduction-band minima at the K point, and the band edge at 1.35 eV to the conduction-band minimum at Q (Supplementary Figure 10). With these assignments, we assert that mWSe₂ is an indirect band-gap and weakly doped *p*-type semiconductor, whose quasiparticle energy gap is as large as $E_g = 2.56$ eV and exciton binding energy $E_B = 0.82$ eV ($E_{opt} = 1.724$ eV).^{15,27} Furthermore, SOC-split conduction bands at K are found to be $\Delta_{SO,C}(\text{mWSe}_2) = 0.03$ eV. Recently, Wang *et al.* reported the similar value ($\Delta_{SO,C}(\text{mWSe}_2) \approx 0.04$ eV) by optical reflectance and PL spectroscopy measurements.³⁵

Although the rather moderate dI/dV_b progression of the mMoSe₂ film is similar to the spectrum from the misaligned mWSe₂ device, a tunnel feature corresponding to the SOC-split lower valence-band edge at K is readily identified at -1.79 eV in both regular and normalized dI/dV_b (Figure 3c). Consequently, the higher SOC-split valence-band edge can be assigned at -1.59 eV based on the optically obtained $\Delta_{SO}(\text{mMoSe}_2) = 0.20$ eV, and the dI/dV_b crest at -2.13 eV marks the valence-band maximum at Γ . Notably, the mMoSe₂ spectra in the empty states are significantly enhanced in value similar to the mMoS₂, and dI/dV_b becomes realigned to the graphene baseline at ≈ 0.8 eV with a sizable adjustment of tunneling constant (dotted green line in Figure 3c). We assign the conduction-band minimum of the mMoSe₂ at 0.87 eV, which makes mMoSe₂ a direct band-gap *n*-type semiconductor with a quasiparticle energy gap $E_g = 2.46$ eV and an exciton binding energy $E_B = 0.82$ eV ($E_{opt} = 1.638$ eV).

The most common atomic defects in mWSe₂ and mMoSe₂ films are selenium-atom vacancies.¹² Similar to the sulfur vacancies in mWS₂ and mMoS₂, singlet a_1 states are expected to form closer to the valence bands with varying spectral locations in the Se-based TMDs; a_1 states in mWSe₂ mostly form below the valence-band maximum, while the bulk portion of mMoSe₂ a_1 defect states are expected to form inside the energy gap. Augmented dI/dV_b attributed to the a_1 defect states are delineated in purple in Figure 3a and 3c, where the a_1 defect states in mMoSe₂ extend further inside the energy gap while the area relating to the mWSe₂ a_1 defect states is apparently narrower. Doublet e defect states from the missing selenium atoms are expected to form mid-gap states inside the energy gaps, with corresponding tunnel spectra of mWSe₂ identified from the dI/dV_b bumps inside the energy gap (red arrows in Figure 3a & Supplementary Figure 8). The amplified and extended dI/dV_b of mMoSe₂, over which the e defect states are known to exist, suggest that selenium vacancies are more prevalent in mMoSe₂ than mWSe₂, and some of them tend to form vacancy chains or clusters.

Comparison of the atomic defect states in SC-mTMDs. We numerically calculate the atomic defect DOS from chalcogen-atom vacancies in the four SC-mTMDs with a consideration of the SOC effect, and present overlaid plots with experimental data in Figure 4a. In these calculations, we do not consider Coulombic many-body effects since a rather simplified DFT is sufficient enough to explain the atomic defect states in SC-mTMDs. It is crucial to note that the SOC effect influences not only the intrinsic electronic structures but also the defect states from chalcogen-atom vacancies.³⁶ As displayed in Figure 4a, the SOC effect splits e defect states by ≈ 0.2 eV in mWS₂ and mWSe₂, while the splitting is minimal in mMoS₂ and mMoSe₂ (Supplementary Figure 11). As experimentally and theoretically confirmed, the a_1 defect states of the Mo-based films

extend further into the energy gap, while the majority of the a_1 states of the W-based films hide under the valence bands. Spectral locations of the doublet e defect states in mWS_2 and $mWSe_2$ are close to the theoretical expectations, and calculated e states in $mMoS_2$ and $mMoSe_2$ are in the vicinity of the expanded defect-induced dI/dV_b . We additionally calculate the defect DOS by double chalcogen-atom vacancies ($V_S V_S$ or $V_{Se} V_{Se}$) and present them with dotted grey lines in Figure 4a. As noted previously, the $e-e$ divacancy defects become hybridized and form additional mid-gap states inside the energy gap, further extended toward the conduction-band edge in SC-mTMDs. We consider charge neutral chalcogen-atom vacancies in our calculations, and find that the calculated spectral locations of both a_1 and e states in $mMoS_2$, $mMoSe_2$, and mWS_2 films are consistently shifted to higher energies than the experimentally identified positions, with the sole exception being the e defects in the weakly p -doped $mWSe_2$. Such consistent energy-level shifting of a_1 and e defect states to higher energies (toward conduction bands) presents a strong experimental implication that chalcogen-atom vacancies in SC-mTMDs can work as dopants, especially as dominant donor states in mWS_2 , $mMoS_2$, and $mMoSe_2$ films.

Here, it is worth mentioning that there could exist several other defects in the SC-mTMDs such as H_2 or N_2 adatoms, transition metal-atom vacancies, or others. However, experimental identifications of such scant defects are daunting, especially in our planar junctions where active areas are as large as several microns in dimension. The observed mid-gap states are ensembles of all the available defects, whose spectra could be easily overshadowed by the more abundant defect sources; missing chalcogen atoms in S- and Se-based SC-mTMDs. Moreover, the formation energies of chalcogen-atom vacancies are favorable to many other defects. For example, much higher formation energies of transition-metal atom vacancies suggest that the missing transition-metal atoms are not energetically favorable to chalcogen-atom vacancies, not to mention that the

spectral locations of such defects are different in energy from those of chalcogen-atom vacancies (Supplementary Figure 12).^{8,11,37,38} In addition, we find that the binding energies of H on SC-TMDs are negative with respect to free H₂ molecules; -1.9 , -2.1 , -2.2 and -2.4 eV/H, respectively for MoS₂, MoSe₂, WS₂ and WSe₂, as similar to N₂ chemisorption,^{37,38} suggesting that H atoms are more likely to desorb from the TMDs and form H₂ molecules instead. The calculated binding energies of H₂ on the surface of TMD films are a few tens of meV, which allow H₂ to be easily detached from the SC-TMD films as well.

To further clarify the similarities and dissimilarities regarding atomic defect states in SC-mTMDs, we calculate the formation energies ($E_{\text{VS},\text{VSe}}$) of individual chalcogen-atom vacancies in the four films (Figure 4b). Our calculations suggest that sulfur atoms are relatively easier to be taken off with lower atomic-defect formation energies than selenium atoms, implying that mMoS₂ ($E_{\text{VS}}(\text{mMoS}_2) = 1.267$ eV) would have the most chalcogen-atom vacancies in total, while mWSe₂ ($E_{\text{VSe}}(\text{mWSe}_2) = 1.668$ eV) would be the least vulnerable to losing selenium atoms. Moreover, we can deduce the density of states of chalcogen-atom vacancies in the intrinsic SC-mTMDs, revealing that mMoS₂ has the highest defect DOS with $D_{\text{VS}}(\text{mMoS}_2) = 1.46 \times 10^{12}$ cm⁻², followed by mWS₂ ($D_{\text{VS}}(\text{mWS}_2) = 6.95 \times 10^{11}$ cm⁻²), mMoSe₂ ($D_{\text{VS}}(\text{mMoSe}_2) = 3.51 \times 10^{11}$ cm⁻²), and finally mWSe₂ with the lowest DOS at $D_{\text{VS}}(\text{mWSe}_2) = 1.31 \times 10^{11}$ cm⁻².

Intriguingly, tunneling spectra related to the doublet e defect states in mWS₂ remain as an isolated dI/dV_b hump (Figure 2a), despite the fact that mWS₂ layers are expected to have a larger defect DOS than mMoSe₂, in which a much extended defect-induced dI/dV_b bump is formed (Figure 3c). Our DFT calculations confirm that sulfur vacancies in mWS₂ films are the least likely to hybridize to form divacancies or vacancy chains, since the vacancy binding energy of mWS₂ is the lowest ($E_{\text{bind}}(\text{mWS}_2) = 0.033$ eV) among the four films (Figure 4c). In comparison, selenium-

atom vacancies in mMoSe₂, with a vacancy-binding energy ($E_{\text{bind}}(\text{mMoSe}_2) = 0.126 \text{ eV}$) one order higher than mWS₂, are expected to form line-type defects or defect clusters with relative ease, leading the mid-gap spectra originating from doublet e defect states to extend wider within the energy gap. Finally, a few dI/dV_b humps for the doublet defect states in the mWSe₂ (Figure 3a) could imply that some selenium-atom vacancies become hybridized, justified by a relatively high vacancy-binding energy ($E_{\text{bind}}(\text{mWSe}_2) = 0.086 \text{ eV}$), although the overall number of selenium-atom vacancies is expected to be the lowest among the four SC-mTMDs. However, we should note that these dI/dV_b bumps could be also attributed to the SOC-induced defect-state splittings, not just the double Se vacancies. At this moment, we cannot say with certainty whether the SOC or divacancy defects or both are the sources for the isolated set of dI/dV_b bumps in mWSe₂, which calls for further theoretical and experimental works.

Discussions

By implementing electron tunneling and optical spectroscopy measurements with DFT analyses, we have provided the most accurate and reliable material parameters to date of four representative SC-mTMD films. Specifically, our work includes spectra profiles of the mid-gap states from individual chalcogen-atom vacancies, quasiparticle energy gaps, and exciton binding energies; all observed key material parameters are summarized in the Table 1. Through such experimental and theoretical studies, we are able to confirm that chalcogen-atom vacancies are the most prevalent atomic defects in SC-mTMDs, and these defects induce two mid-gap states around valence band edges (singlet a_1 states) and inside energy gaps (doublet e states). Atomic defect states reveal similarities and dissimilarities among these four distinctive SC-mTMDs regarding the spectral locations of the defect-induced mid-gap states, physical vacancy formations, and intrinsic defect

DOS. Our studies reveal that S-based mTMDs are more vulnerable to chalcogen-atom vacancies than their Se-based counterparts, presenting strong experimental implications that such vacancies are directly related to charged dopings in SC-mTMDs: S-based films are heavily doped *n*-type semiconductors, while Se-based films configure either as a moderately doped *n*-type semiconductor (mMoSe₂) or a weakly doped *p*-type (or intrinsic) semiconductor (mWSe₂). Competing with the overall defect DOS and vacancy binding energies, chalcogen-atom vacancies in the intrinsic mMoS₂, mMoSe₂, and mWSe₂ films are inclined to form hybridized vacancy chains while sulfur-atom vacancies in mWS₂ films remain isolated. Additionally, we confirm that the energy bands of the films are greatly renormalized by enhanced many-body interactions, and diminished screening effects in the atomically thin 2D structures, leading to exceptionally large excitonic binding energies up to ≥ 0.78 eV. By implementing crystalline angle-dependent electron tunneling spectroscopies, we have demonstrated that tunneling decay constants, and therefore tunnel signals in the 2D vdW heterostructures, can be readily tuned by controlling the tunnel-electron momentums between tunnel probe and SC-mTMD crystals. This provides a useful experimental knob for investigating the electronic structures of various TMDs with much improved measurement accuracy. We believe that the key material parameters presented in this report can provide a solid foundation for current and next-generation electronic and optical applications with ultrathin semiconducting TMD films. Moreover, our experimental approaches can be applicable to any low-dimensional quantum materials and their unlimited combinations for high-precision material metrology.

Methods

Device Fabrication. In our planar vdW heterostructures, preparation of atomically clean interfaces is of critical importance for accurate and reliable material characterization of SC-mTMD films. At first, 60 nm to 100 nm thick high-crystalline *h*-BN flakes are mechanically exfoliated on a 90 nm thick SiO₂ layer on Si substrate. Prior to exfoliation, we thoroughly clean the SiO₂/Si substrates with acetone and IPA in an ultrasonication bath and subsequent dipping in piranha solution. We carefully examine *h*-BN surface cleanness with a dark-filtered optical microscope to avoid cracks and non-uniform *h*-BN layers. Then, single-layer graphene mechanically isolated onto polymer stacks of PMMA (poly(methyl methacrylate)) – PSS (polystyrene sulfonate) layers is transferred to the prelocated *h*-BN flake on SiO₂/Si substrate using a dry transfer method. The total thicknesses of PMMA and PSS films on bare Si substrates are adjusted for optimal optical contrasts to identify the layer number of graphene and tunnel *h*-BN. Once the PMMA/PSS/Si substrates with 2D layers of graphene, *h*-BN, SC-mTMDs, and graphite on the polymer stacks are placed on top of DI water, the water soluble PSS layer is quickly dissolved and the PMMA layer with 2D materials becomes isolated from the Si substrate. Then, with a micromanipulation stage equipped with a rotator and an optical microscope, we transfer the 2D layers on PMMA to a targeted location on a SiO₂/Si substrate with micrometer accuracy. After dissolving PMMA in warm acetone (60 °C), we further anneal the samples in forming gases of Ar and H₂ (9:1 ratio by flow rate). We set the annealing temperature at 350 °C for single-layer graphene and then reduce the temperature to 250 °C for SC-mTMD films to avoid undesired defect-state formations. After annealing, we confirm the surface cleanness with an atomic force microscope. By following a similar dry transfer protocol, SC-mTMD films, thin *h*-BN (3 to 4 layer), and graphite flakes are sequentially transferred on top of the graphite-*h*-BN stack to complete the mTMD-based planar tunneling device. For the second type of planar tunnel devices, we intentionally align the crystalline angles

of the top graphite and monolayer WSe₂. No careful alignments are necessary for transferring thin tunnel *h*-BN and underlying single-layer graphene films. Finally, titanium and gold (5 nm / 95 nm) electrodes are fabricated to electrically connect the top graphite and bottom graphene layers by using standard electron-beam lithography and lift-off procedures. All four high-purity (> 99.995%) SC-TMD crystals were purchased from HQ Graphene with no additional dopants added during growth procedures.

Electrical measurements. All electrical measurements are carried out under a high vacuum condition below 10^{-5} Torr with a cryogen-free probe station and cryogen-free dilution refrigerator, whose base temperatures are 5.7 K and below 100 mK, respectively. We first characterize the electronic properties of our planar tunnel junctions with the probe station, and transfer the working devices to the dilution refrigerator for further in-depth measurements. With SC-mTMD films encapsulated by non-interacting high-quality *h*-BN and graphene, our devices are resilient to multiple thermal circulations. Current-voltage characteristics of the mTMD planar tunnel junctions are measured with a DC voltage source applied to the top graphite and a current amplifier connected to the bottom graphene layer. Voltage output from the current amplifier is monitored through a digital multimeter, and differential conductance (dI/dV_b) is numerically obtained.

Optical measurements. Spectral information regarding the *A*-exciton peaks of the SC-mTMD films is measured with a micro-PL system pumped by a CW Nd: YAG laser at 532 nm. Pump light is vertically shone onto the SC-mTMD flakes through a $\times 50$ objective lens, and the PL signals collected through the same lens are analyzed with a liquid nitrogen-cooled Si CCD detector with 550 nm long pass filter. The spatial extent of the pump laser is confirmed to be 2 μ m in diameter

from knife-edge experiments. Energy splitting between the *A*- and *B*-exciton peaks of the SC-mTMDs is measured with a micro-reflectance spectroscopy setup equipped with a supercontinuum white light source. The diameter of the supercontinuum light source is estimated to be 4 μm . For temperature-dependent PL and reflectance measurements, our mTMD-based planar junctions are mounted in a liquid nitrogen-cooled cryostat.

DFT for atomic defect states. Density functional theory calculations are performed using the Vienna Ab initio Simulation Package (VASP).³⁹ Ions are represented by projector-augmented wave (PAW) potentials,⁴⁰ and generalized gradient approximation (PBE) is employed to describe the exchange-correlation functional.⁴¹ A plane-wave basis set with an energy cutoff of 350 eV is employed to describe electronic wave functions. For defect-state calculations, we use an 8×8 supercell with consideration of the dipole, and the Γ point for Brillouin-zone integration is used for structural optimizations and total energy calculations. We find that the effects from the dipole correction are very small, with an energy difference of less than 1 meV for mMoS₂ (Supplementary Figure 12). The calculated hexagonal lattice constants of mMoS₂, mMoSe₂, mWS₂, and mWSe₂ are 3.188 Å, 3.312 Å, 3.179 Å, and 3.325 Å, respectively. The atomic positions of all clusters are relaxed with residual forces smaller than 0.01 eV/Å.

Data availability

All data supporting the findings of this study are available from the corresponding authors on request.

References

1. Srivastava, A., Sidler, M., Allain, A. V., Lembke, D. S., Kis, A. & Imamoglu, A. Optically active quantum dots in monolayer WSe₂. *Nat. Nanotechnol.* **10**, 491–496 (2015).
2. He, Y.-M., Clark, G., Schaibley, J. R., He, Y., Chen, M.-C., Wei, Y.-J., Ding, X. Zhang, Q., Yao, W., Xu, X., Lu, C.-Y. & Pan, J.-W. Single quantum emitters in monolayer semiconductors. *Nat. Nanotechnol.* **10**, 497–502 (2015).
3. Koperski, M., Nogajewski, K., Arora, A., Cherkez, V., Mallet, P., Veuillen, J.-Y., Marcus, J., Kossacki, P. & Potemski, M. Single photon emitters in exfoliated WSe₂ structures. *Nat. Nanotechnol.* **10**, 503–506 (2015).
4. Chakraborty, C., Kinnischtzke, L., Goodfellow, K. M., Beams, R. & Vamivakas, A. N. Voltage-controlled quantum light from an atomically thin semiconductor. *Nat. Nanotechnol.* **10**, 507–511 (2015).
5. Lu, S.-C. & Leburton, J.-P. Electronic structures of defects and magnetic impurities in MoS₂ monolayers. *Nanoscale Res. Lett.* **9**, 676 (2014).
6. Hong, J., Jin, C., Yuan, J. & Zhang, Z. Atomic Defects in Two-Dimensional Materials: From Single-Atom Spectroscopy to Functionalities in Opto-/Electronics, Nanomagnetism, and Catalysis. *Adv. Mater.* **29**, 1606434 (2017).
7. Hong, J., Hu, Z., Probert, M., Li, K., Lv, D., Yang, X., Gu, L., Mao, N., Feng, Q., Xie, L., Zhang, J., Wu, D., Zhang, Z., Jin, C., Ji, W., Zhang, X., Yuan, J. & Zhang, Z. Exploring atomic defects in molybdenum disulphide monolayers. *Nat. Commun.* **6**, 6293 (2015).

8. Noh, J. Y., Kim, H. & Kim, Y. S. Stability and electronic structures of native defects in single-layer MoS₂. *Phys. Rev. B* **89**, 205417 (2014).
9. Ghorbani-Asl, M., Enyashin, A. N., Kuc, A., Seifert, G. & Heine, T. Defect-induced conductivity anisotropy in MoS₂ monolayers. *Phys. Rev. B* **88**, 245440 (2013).
10. Guo, Y., Liu, D. & Robertson, J. Chalcogen vacancies in monolayer transition metal dichalcogenides and Fermi level pinning at contacts. *Appl. Phys. Lett.* **106**, 173106 (2015).
11. Zhou, W., Zou, X., Najmaei, S., Liu, Z., Shi, Y., Kong, J., Lou, J., Ajayan, P. M., Yakobson, B. I. & Idrobo, J.-C. Intrinsic structural defects in monolayer molybdenum disulfide. *Nano Lett.* **13**, 2615–2622 (2013).
12. Lin, Z., Carvalho, B. R., Kahn, E., Lv, R., Rao, R., Terrones, H., Pimenta, M. A. & Terrones, M. Defect engineering of two-dimensional transition metal dichalcogenides. *Defect engineering of two-dimensional transition metal dichalcogenides. 2D Mater.* **3**, 022002 (2016).
13. Patra, T. K., Zhang, F., Schulman, D. S., Chan, H., Cherukara, M. J., Terrones, M., Das, S., Narayanan, B. & Sankaranarayanan, S. K. R. S. Defect Dynamics in 2-D MoS₂ Probed by Using Machine Learning, Atomistic Simulations and High-Resolution Microscopy. *ACS Nano* **12**, 8006–8016 (2018).
14. Chen, Y., Huang, S., Ji, X., Adepalli, K., Yin, K., Ling, X., Wang, X., Xue, J., Dresselhaus, M., Kong, J. & Yildiz, B. Tuning Electronic Structure of Single Layer MoS₂ through Defect and Interface Engineering. *ACS Nano* **12**, 2569–2579 (2018).

15. Zhang, C., Gong, C., Nie, Y., Min, K.-Y., Liang, C., Oh, Y. J., Zhang, H., Wang, W., Hong, S., Colombo, L., Wallace, R. M. & Cho, K. Systematic study of electronic structure and band alignment of monolayer transition metal dichalcogenides in Van der Waals heterostructures. *2D Mater.* **4**, 015026 (2017).
16. Brumme, T., Calandra, M. & Mauri, F. First-principles theory of field-effect doping in transition-metal dichalcogenides: Structural properties, electronic structure, Hall coefficient, and electrical conductivity. *Phys. Rev. B* **91**, 155436 (2015).
17. Ugeda, M. M., Bradley, A. J., Shi, S.-F., da Jornada, F. H., Zhang, Y., Qiu, D. Y., Ruan, W., Mo, S.-K., Hussain, Z., Shen, Z.-X., Wang, F., Louie, S. G. & Crommie, M. F. Giant bandgap renormalization and excitonic effects in a monolayer transition metal dichalcogenide semiconductor. *Nat. Mater.* **13**, 1091–1095 (2014).
18. Zhang, C., Chen, Y., Johnson, A., Li, M.-Y., Li, L.-J., Mende, P. C., Feenstra, R. M. & Shih, C.-K. Probing Critical Point Energies of Transition Metal Dichalcogenides: Surprising Indirect Gap of Single Layer WSe₂. *Nano Lett.* **15**, 6494–6500 (2015).
19. Zhang, C., Johnson, A., Hsu, C.-L., Li, L.-J. & Shih, C.-K. Direct Imaging of Band Profile in Single Layer MoS₂ on Graphite: Quasiparticle Energy Gap, Metallic Edge States, and Edge Band Bending. *Nano Lett.* **14**, 2443–2447 (2014).
20. Yankowitz, M., McKenzie, D. & Leroy, B. J. Local Spectroscopic Characterization of Spin and Layer polarization in WSe₂. *Phys. Rev. Lett.* **115**, 136803 (2015).
21. Chiu, M.-H., Zhang, C., Shiu, H.-W., Chuu, C.-P., Chen, C.-H., Chang, C.-Y. S., Chen, C.-H., Chou, M.-Y., Shih, C.-K. & Li, L.-J. Determination of band alignment in the single-layer MoS₂/WSe₂ heterojunction. *Nat. Commun.* **6**, 7666 (2015).

22. Jung, S., Myoung, N., Park, J., Jeong, T. Y., Kim, H., Watanabe, K., Taniguchi, T., Ha, D. H., Hwang, C. & Park, H. C. Direct Probing Electronic Structures of Single and Bilayer Graphene with Hexagonal Boron Nitride Tunneling Barrier. *Nano Lett.* **17**, 206–213 (2017).
23. Kim, H., Leconte, N., Chittari, B. L., Watanabe, K., Taniguchi, T., MacDonald, A. H., Jung, J & Jung, S. Accurate Gap Determination in Monolayer and Bilayer Graphene/*h*-BN Moiré Superlattices. *Nano Lett.* **18**, 7732–7741 (2018).
24. Jung, S., Park, M., Park, J., Jeong, T. Y., Kim, H.-J., Watanabe, K., Taniguchi, T., Ha, D. H., Hwang, C. & Kim, Y.-S. Vibrational Properties of *h*-BN and *h*-BN-Graphene Heterostructures Probed by Inelastic Electron Tunneling Spectroscopy. *Sci. Rep.* **5**, 16642 (2015).
25. O'Donnell, K. P. & Chen, X. Temperature dependence of semiconductor band gaps. *Appl. Phys. Lett.* **58**, 2924–2926 (1991).
26. McDonnell, L. P., Huang, C.-C., Cui, Q., Hewak, D. W. & Smith, D. C. Probing Excitons, Trions, and Dark Excitons in Monolayer WS₂ Using Resonance Raman Spectroscopy. *Nano Lett.* **18**, 1428–1434 (2018).
27. Liang, Y., Huang, S., Soklaski, R. & Yang, L. Quasiparticle band-edge energy and band offsets of monolayer of molybdenum and tungsten chalcogenides. *Appl. Phys. Lett.* **103**, 042106 (2013).
28. Komsa, H.-P., Kurasch, S., Lehtinen, O., Kaiser, U. & Krasheninnikov, A. V. From point to extended defects in two-dimensional MoS₂: Evolution of atomic structure under electron irradiation. *Phys. Rev. B* **88**, 035301 (2013).

29. Vancsó, P., Magda, G. Z., Pető, J., Noh, J.-Y., Kim, Y.-S., Hwang, C. Biró, L. P. & Tapasztó, L. The intrinsic defect structure of exfoliated MoS₂ single layers revealed by Scanning Tunneling Microscopy. *Sci. Rep.* **6**, 29726 (2016).
30. Britnell, L., Gorbachev, R. V., Geim, A. K., Ponomarenko, L. A., Mishchenko, A., Greenaway, M. T., Fromhold, T. M., Novoselov, K. S. & Eaves, L. Resonant tunnelling and negative differential conductance in graphene transistors. *Nat. Commun.* **4**, 1794 (2013).
31. Mishchenko, A., Tu, J. S., Cao, Y., Gorbachev, R. V., Wallbank, J. R., Greenaway, M. T., Morozov, V. E., Morozov, S. V., Zhu, M. J., Wong, S. L., Withers, F., Woods, C. R., Kim, Y.-J., Watanabe, K., Taniguchi, T., Vdovin, E. E., Makarovskiy, O., Fromhold, T. M., Fal'ko, V. I., Geim, A. K., Eaves, L. & Novoselov, K. S. Twist-controlled resonant tunnelling in graphene/boron nitride/graphene heterostructures. *Nat. Nanotechnol.* **9**, 808–813 (2014).
32. Greenaway, M. T., Vdovin, E. E., Mishchenko, A., Makarovskiy, O., Patané, A., Wallbank, J. R., Cao, Y., Kretinin, A. V., Zhu, M. J., Morozov, S. V., Fal'ko, V. I., Novoselov, K. S., Geim, A. K., Fromhold, T. M. & Eaves, L. Resonant tunneling between the chiral Landau states of twisted graphene lattices. *Nat. Physics* **11**, 1057–1062 (2015).
33. Wallbank, J. R., Ghazaryan, D., Misra, A., Cao, Y., Tu, J. S., Piot, B. A., Potemski, M., Pezzini, S., Wiedmann, S., Zeitler, U., Lane, T. L. M., Morozov, S. V., Greenaway, M. T., Eaves, L., Geim, A. K., Fal'ko, V. I. Novoselov, K. S. & Mishchenko, A. Tuning the valley and chiral quantum state of Dirac electrons in van der Waals heterostructures. *Science* **353**, 575–579 (2016).

34. Partoens, B. & Peeters, F. M. From graphene to graphite: Electronic structure around the K point. *Phys. Rev. B* **74**, 0745404 (2006).
35. Wang, Z., Zhao, L., Mak, K. F. & Shan, J. Probing the Spin-Polarized Electronic Band Structure in Monolayer Transition Metal Dichalcogenides by Optical Spectroscopy. *Nano Lett.* **17**, 740–746 (2017).
36. Schuler, B., Qiu, D. Y., Refaely-Abramson, S., Kastl, C., Chen, C. T., Barja, S. & Koch, R. J. Large spin-orbit splitting of deep in-gap defect states of engineered sulfur vacancies in monolayer WS₂. Preprint at <https://arxiv.org/abs/1810.02896> (2018).
37. Haldar, S., Vovusha, H., Yadav, M. K., Eriksson, O. & Sanyal, B. Systematic study of structural, electronic, and optical properties of atomic-scale defects in the two-dimensional transition metal dichalcogenides MX₂ (M = Mo, W; X = S, Se, Te). *Phys. Rev. B* **92**, 235408 (2015).
38. Ma, D., Ma, B., Lu, Z., He, C., Tang, Y., Lu, Z. & Yang, Z. Interaction between H₂O, N₂, CO, NO, NO₂ and N₂O molecules and a defective WSe₂ monolayer. *Phys. Chem. Chem. Phys.* **19**, 26022–26033 (2017).
39. Kresse, G. & Furthmüller, J. Efficient iterative schemes for ab initio total-energy calculations using a plane-wave basis set. *Phys. Rev. B* **54**, 11169–11186 (1996).
40. Joubert, D. From ultrasoft pseudopotentials to the projector augmented-wave method. *Phys. Rev. B* **59**, 1758–1775 (1999).
41. Perdew, J. P., Burke, K. & Ernzerhof, M. Generalized gradient approximation made simple. *Phys. Rev. Lett.* **77**, 3865–3868 (1996).

Acknowledgments This work was supported by a research grant for the Development of Converging Measurement Technology for Nanotechnology (KRISS-2018-GP2018-0019) funded by the Korea Research Institute of Standards and Science. This work was also supported by the Basic Science Research Program (NRF-2016R1A2B4008816 and NRF-2019R1A2C2004007) through the National Research Foundations of Korea.

Author contributions T.Y.J., H.K., and S.J. fabricated devices and performed electron tunneling spectroscopy measurements. T.Y.J. and K.J.Y. carried out optical spectroscopy measurements, S-J. C. established an electron tunneling model of vertical 2D vdW heterostructures, and Y-S. K. performed DFT calculations. High quality *h*-BN crystals were synthesized by K.W. and T.T.. T.Y.J., H.K., K.J.Y, S-J. C. Y.-S.K. and S.J. contributed in analyzing data and preparing the manuscript.

Additional information The authors declare no competing interests. Correspondence and requests for materials should be addressed to Y.-S. K. or S. J.

Figure Captions

Figure 1 | Electron tunneling and optical spectroscopy studies with SC-mTMD vdW heterostructures. **a**, Schematic and optical viewgraph of our mTMD-based vdW planar heterostructure for electron tunneling and optical spectroscopy measurements. For electron tunneling studies, sample-bias voltage (V_b) is applied to the top graphite, and tunneling current through the *h*-BN and SC-mTMD is monitored at the bottom graphene. For optical spectroscopy measurements, a laser with either continuous 532 nm for PL or supercontinuum white sources for reflectance measurements is incident vertically on the mTMD planar tunnel device, and optical signals are collected with a $\times 50$ objective lens. **b**, Simplified energy-band alignments of our SC-mTMD-based planar tunnel junctions. Electrons injected from the graphite probe detect either the SC-mTMD or the bottom graphene layer depending on V_b and its relative position with respect to the mTMD electronic structures. **c**, Representative energy-momentum dispersion relations for SC-mTMD films depicted with key material parameters: atomic defect states (a_1 , e), quasiparticle (E_g) and optical (E_{opt}) energy gaps, exciton binding energy (E_B), and others. **d**, Series of differential conductance ($G = dI/dV_b$) curves as a function of V_b from mWS₂ (blue), mMoS₂ (red), mWSe₂ (green), and mMoSe₂ (orange) planar tunnel junctions at $T \leq 4$ K. Arrows respectively represent the locations of the quasiparticle energy gaps. Inset: A representative dI/dV_b spectrum from one

of the planar graphite–*h*-BN–graphene tunnel junctions. Green lines indicate numerical fittings to experimental data (red circles). **e**, Collection of PL spectra from the SC-mTMD planar devices at $T = 300$ K (dotted lines) and $T = 80$ K (solid lines). Inset: Reflectance spectra measured at $T = 300$ K (dotted lines) and $T = 80$ K (solid lines) from the mWS₂ planar tunnel device.

Figure 2 | Detailed electronic structure analyses from electron-tunneling spectroscopy measurements of S-based mTMDs. **a, c**, Tunnel spectra plotted with dI/dV_b in log scale from the mWS₂ (**a**) and mMoS₂ (**c**) planar tunnel junctions. Solid and dotted green lines mark the graphene baselines. Normalized conductance $(dI/dV_b)/(I/V_b)$ plots (blue solid lines) better represent tunneling spectra features at higher V_b . The areas delineated with purple and orange respectively represent the a_1 and e defect states from sulfur-atom vacancies. dI/dV_b spectral locations and key electronic structure assignments for the mWS₂ (**a**) and mMoS₂ (**c**) films are marked with dotted black lines and solid red arrows. **b, d**, Summarized energy-level assignments for the mWS₂ (**b**) and mMoS₂ (**d**) films. Uncertainty for each energy-level assignment is less than ± 0.01 eV.

Figure 3 | Detailed electronic structure analyses from electron-tunneling spectroscopy measurements of Se-based mTMDs. **a, c**, Tunnel spectra plotted with dI/dV_b in log scale from the mWSe₂ (**a**) and mMoSe₂ (**c**) planar tunnel junctions. Tunnel spectra from the crystallographically aligned device are delineated with solid orange lines, and negative dI/dV_b features for resonant tunneling are marked with green circles. Solid and dotted green lines indicate the graphene baseline spectra. The areas delineated with purple and orange respectively represent the a_1 and e defect states from selenium-atom vacancies. **b, d**, Summarized energy-level assignments for the mWSe₂ (**b**) and mMoSe₂ (**d**) films. Uncertainty for each energy-level assignment is less than ± 0.01 eV.

Figure 4 | DFT studies on chalcogen-atom vacancies in SC-mTMDs. **a**, DFT-calculated locations and density of states of charge-neutral a_1 and e defect-states from single chalcogen-atom vacancies in the four SC-mTMD films with a consideration of the SOC effect. The defect DOS induced by double chalcogen-atom vacancies are overlaid with dotted grey lines. Tops of the valence-band edges are set at 0 eV. Note that quasiparticle energy gaps from DFT calculations are severely underestimated without the consideration of electron–electron interactions. Experimentally identified a_1 and e defect states are respectively overlaid with brown and orange shadows. **b, c**, Formation ($E_{vs, vse}$, **b**) and binding (E_{bind} , **c**) energies of individual chalcogen-atom vacancies in the four representative films.

Table 1 | Experimentally identified material parameters of the four representative SC-mTMDs. All parameters listed are experimentally addressed by electron tunneling and optical spectroscopy measurements with SC-mTMD-based planar heterostructures. Energy level assignments have uncertainty levels of less than ± 0.01 eV.

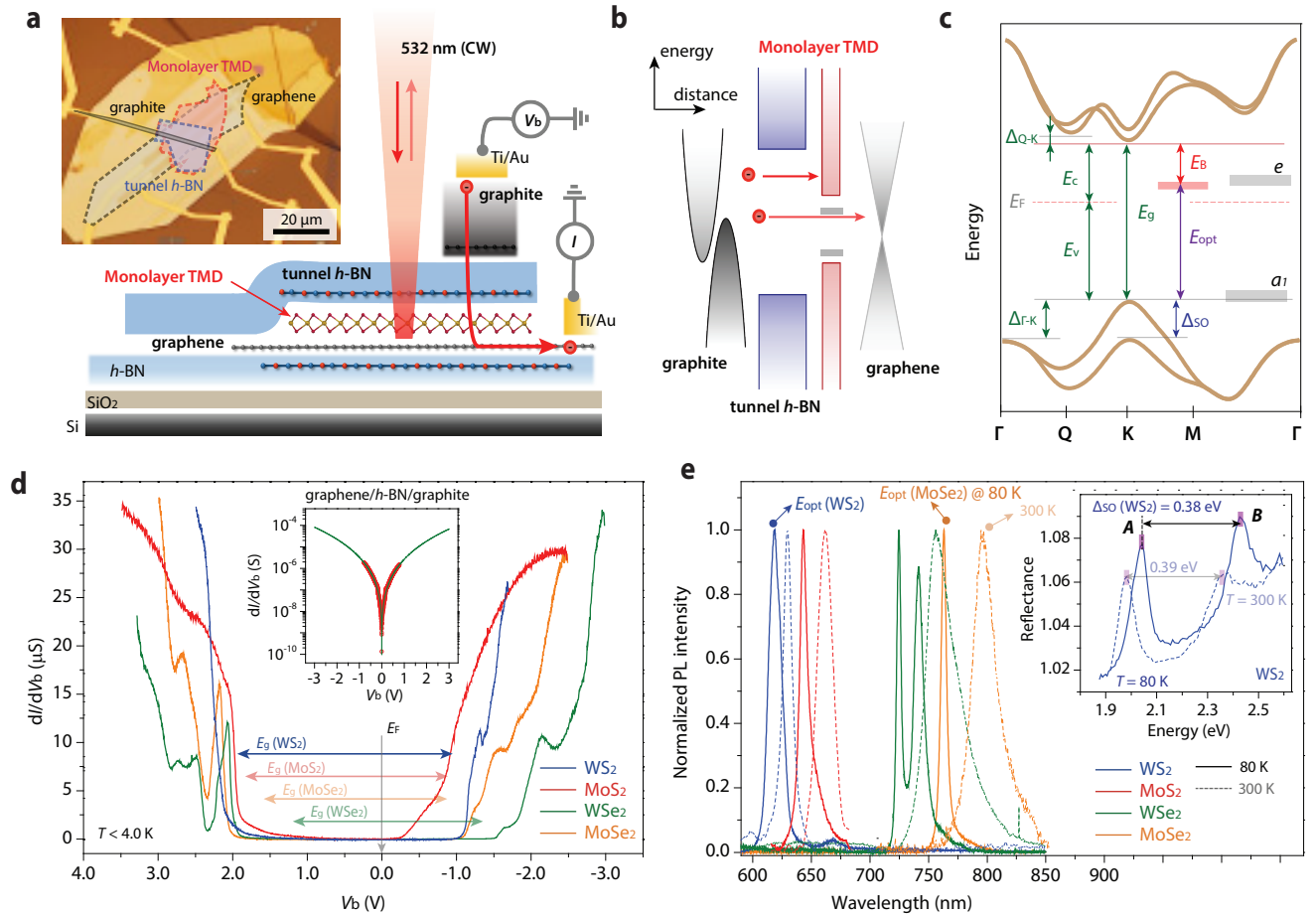


Figure 1: Electron tunneling and optical spectroscopy studies with SC-mTMD vdW heterostructures. (a) Schematic and optical viewgraph of our mTMD-based vdW planar heterostructures for electron tunneling and optical spectroscopy measurements. For electron tunneling studies, sample-bias voltage (V_b) is applied to the top graphite, and tunneling current through the *h*-BN and SC-mTMD is monitored at the bottom graphene. For optical spectroscopy measurements, a laser with either continuous 532 nm for PL or supercontinuum white sources for reflectance measurements is incident vertically on the mTMD planar tunnel devices, and optical signals are collected with a $\times 50$ objective lens. (b) Simplified energy-band alignments of our SC-mTMD-based planar tunnel junctions. Electrons injected from the graphite probe detect either the SC-mTMD or the bottom graphene layer depending on V_b and its relative position with respect to the mTMD electronic structures. (c) Representative energy-momentum dispersion relations for SC-mTMD films depicted with key material parameters: atomic defect states (a_1 , e), quasiparticle (E_g) and optical (E_{opt}) energy gaps, exciton binding energy (E_B), and others. (d) Series of differential conductance ($G = dI/dV_b$) curves as a function of V_b from mWS₂ (blue), mMoS₂ (red), mWSe₂ (green), and mMoSe₂ (orange) planar tunnel junctions at $T \leq 4$ K. Arrows respectively represent the locations of the quasiparticle energy gaps. Inset: A representative dI/dV_b spectrum from one of the planar graphite-h-BN-graphene tunnel junctions. Green lines indicate numerical fittings to experimental data (red circles). (e) Collection of PL spectra from the SC-mTMDs planar devices at $T = 300$ K (dotted lines) and $T = 80$ K (solid lines). Inset: Reflectance spectra measured at $T = 300$ K (dotted lines) and $T = 80$ K (solid line) from the mWS₂ planar tunnel device.

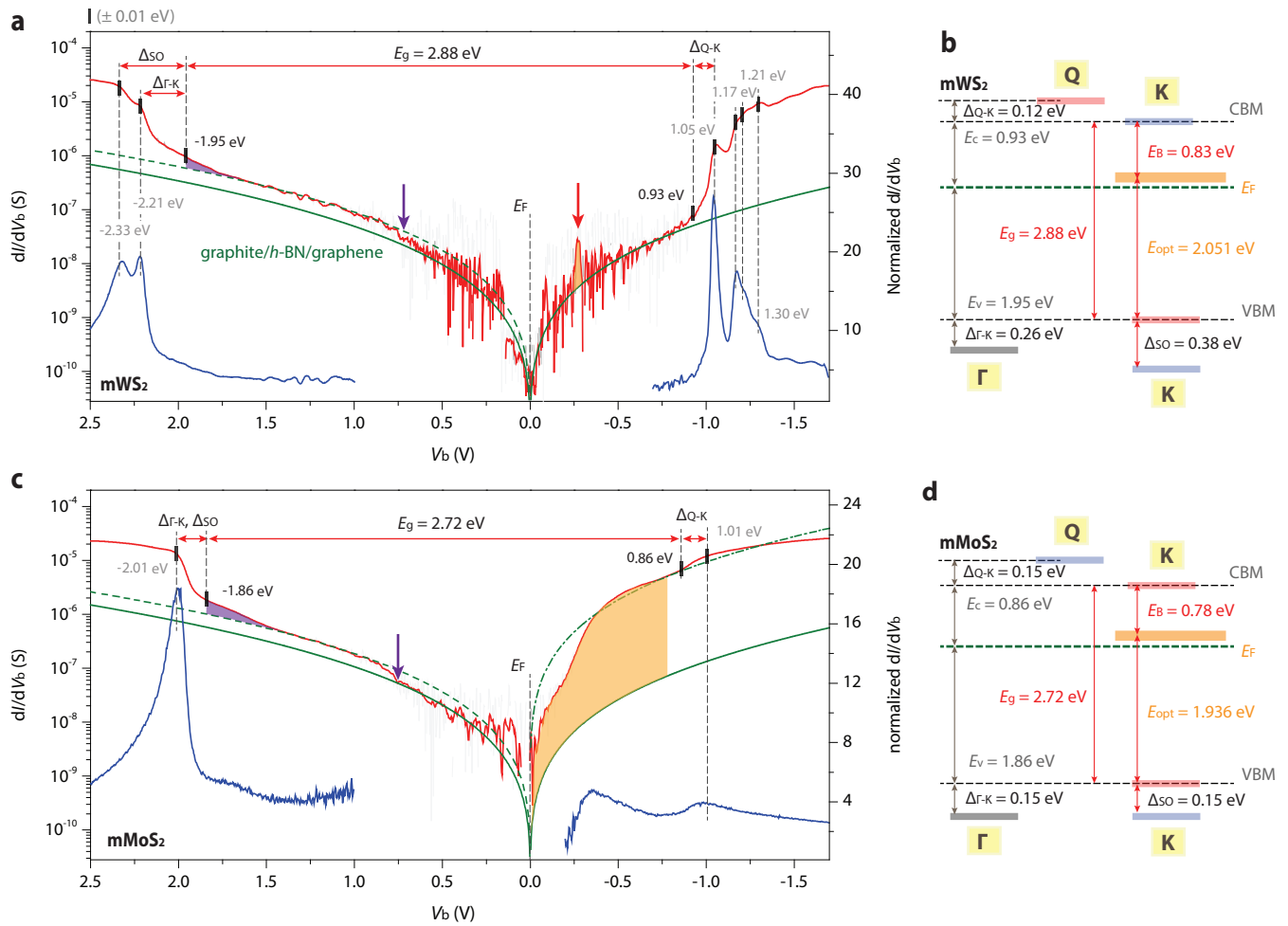


Figure 2: Detailed electronic structure analyses from electron-tunneling spectroscopy measurements for S-based mTMDs. (a, c) Tunnel spectra plotted with dI/dV_b in log scale from the mWS₂ (a) and mMoS₂ (c) planar tunnel junctions. Solid and dotted green lines mark the graphene baselines. Normalized conductance (dI/dV_b)/(I/V_b) plots (blue solid lines) better represent tunneling spectra features at higher V_b . The areas delineated with purple and orange respectively represent the a_1 and e defect states from sulfur-atom vacancies. dI/dV_b spectral locations and key electronic structure assignments for the mWS₂ (a) and mMoS₂ (c) films are marked with dotted black lines and solid red arrows. (b, d) Summarized energy-level assignments for the mWS₂ (b) and mMoS₂ (d) films. Uncertainty for each energy-level assignment is less than ± 0.01 eV.

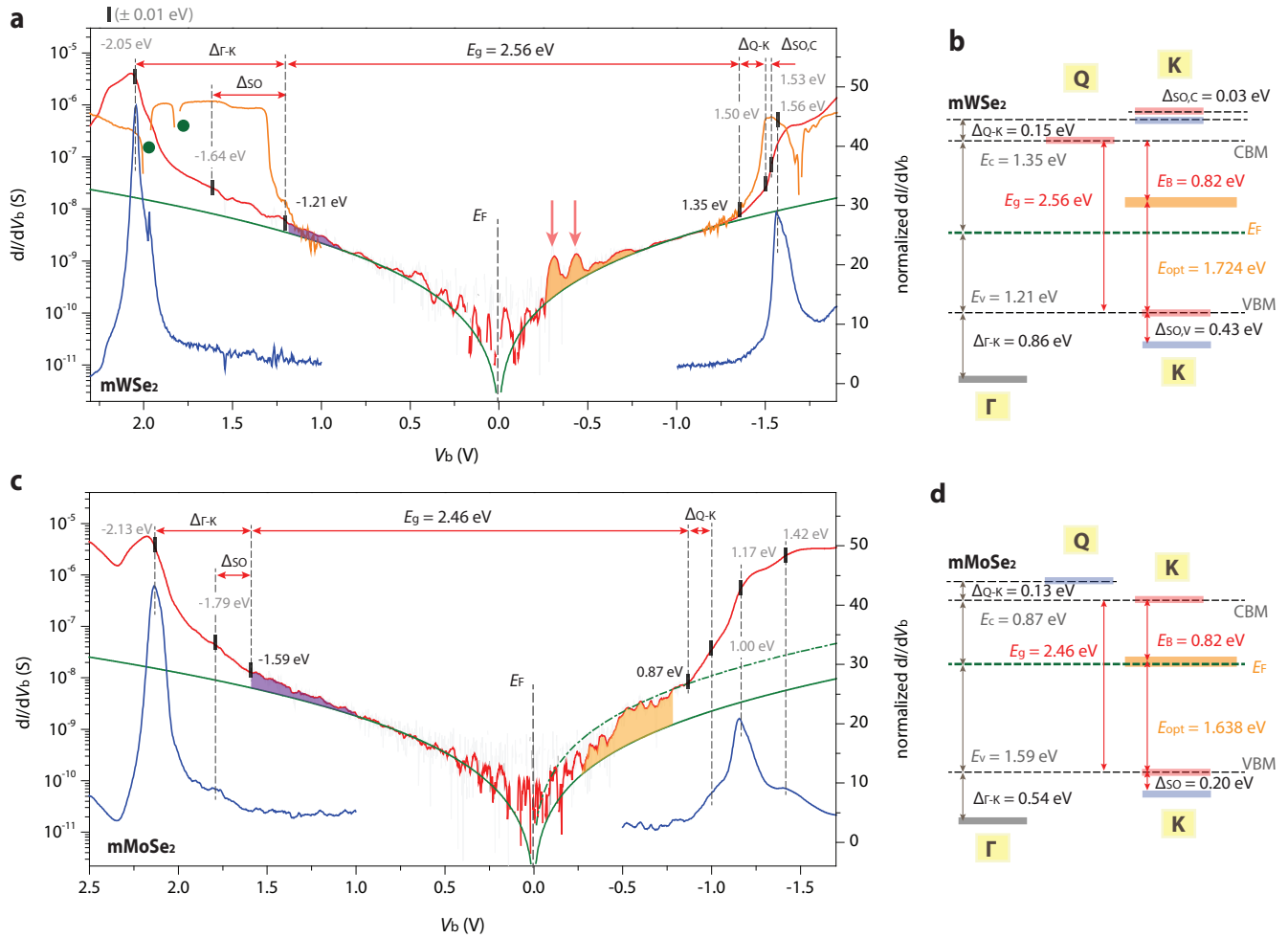


Figure 3: Detailed electronic structure analyses with electron-tunneling spectroscopy measurements for Se-based mTMD films. (a, c) Tunnel spectra plotted with dI/dV_b in log scale from the $mWSe_2$ (a) and $mMoSe_2$ (c) planar tunnel junctions. Tunnel spectra from the crystallographically aligned device are delineated with solid orange lines, and negative dI/dV_b features for resonant tunneling are marked with green circles. Solid and dotted green lines indicate the graphene baseline spectra. The areas delineated with purple and orange respectively represent the a_1 and e defect states from selenium-atom vacancies. (b, d) Summarized energy-level assignments for the $mWSe_2$ (b) and $mMoSe_2$ (d) films. Uncertainty for each energy-level assignment is less than ± 0.01 eV.

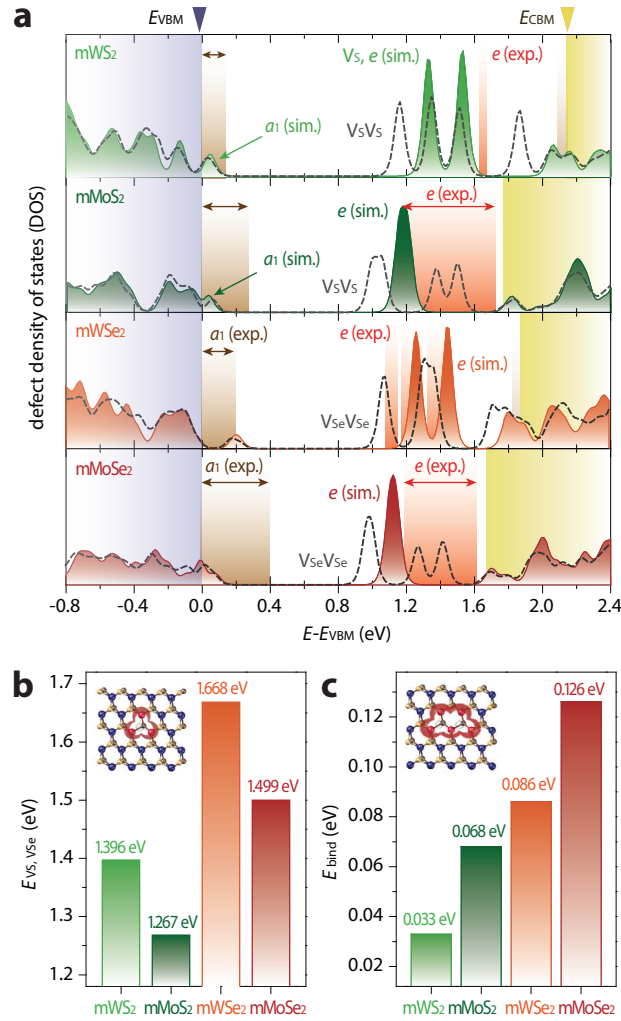


Figure 4: DFT studies on chalcogen-atom vacancies in SC-mTMDs. (a) DFT-calculated locations and density of states of charge-neutral a_1 and e defect-states from single chalcogen-atom vacancies in the four SC-TMD films with a consideration of the SOC effect. The defect DOS induced by double chalcogen-atom vacancies are overlaid with dotted grey lines. Tops of valence-band edges are set at 0 eV. Note that quasiparticle energy gaps from DFT calculations are severely underestimated without the consideration of electron-electron interactions. Experimentally identified a_1 and e defect states are respectively overlaid with brown and orange shadows. (b, c) Formation ($E_{V_s, V_{Se}}$, b) and binding (E_{bind} , c) energies of individual chalcogen-atom vacancies in the four representative films.

(units : eV)

	E_g	E_v	E_c	Δ_{so}	$\Delta_{\kappa\Gamma}(VB)$	$\Delta_{\kappa Q}(CB)$	E_{opt}	E_B
WS₂	2.88	1.95	0.93	0.38	0.26	0.12	2.051	0.83
MoS₂	2.72	1.86	0.86	0.15	0.15	0.15	1.936	0.78
WSe₂	2.56	1.21	1.35	0.43	0.86	-0.15	1.724	0.82
MoSe₂	2.46	1.59	0.87	0.20	0.54	0.13	1.638	0.82

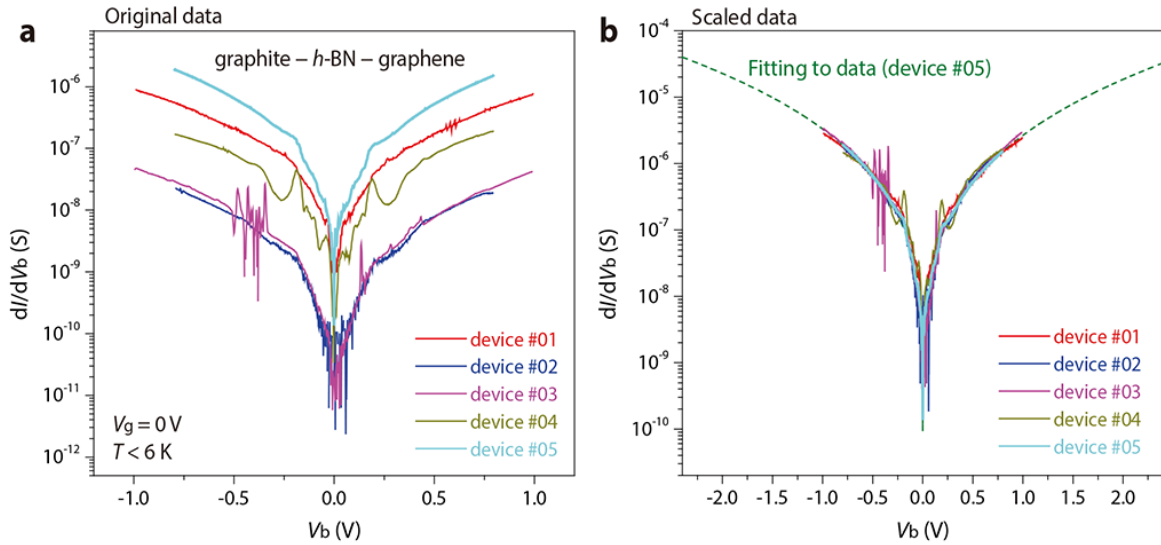
Table 1: Experimentally identified material parameters of the four representative SC-mTMDs. All parameters listed are experimentally addressed by electron tunneling and optical spectroscopy measurements with SC-mTMD-based planar heterostructures. Energy level assignments have uncertainty level of less than ± 0.01 eV.

Supplementary Information

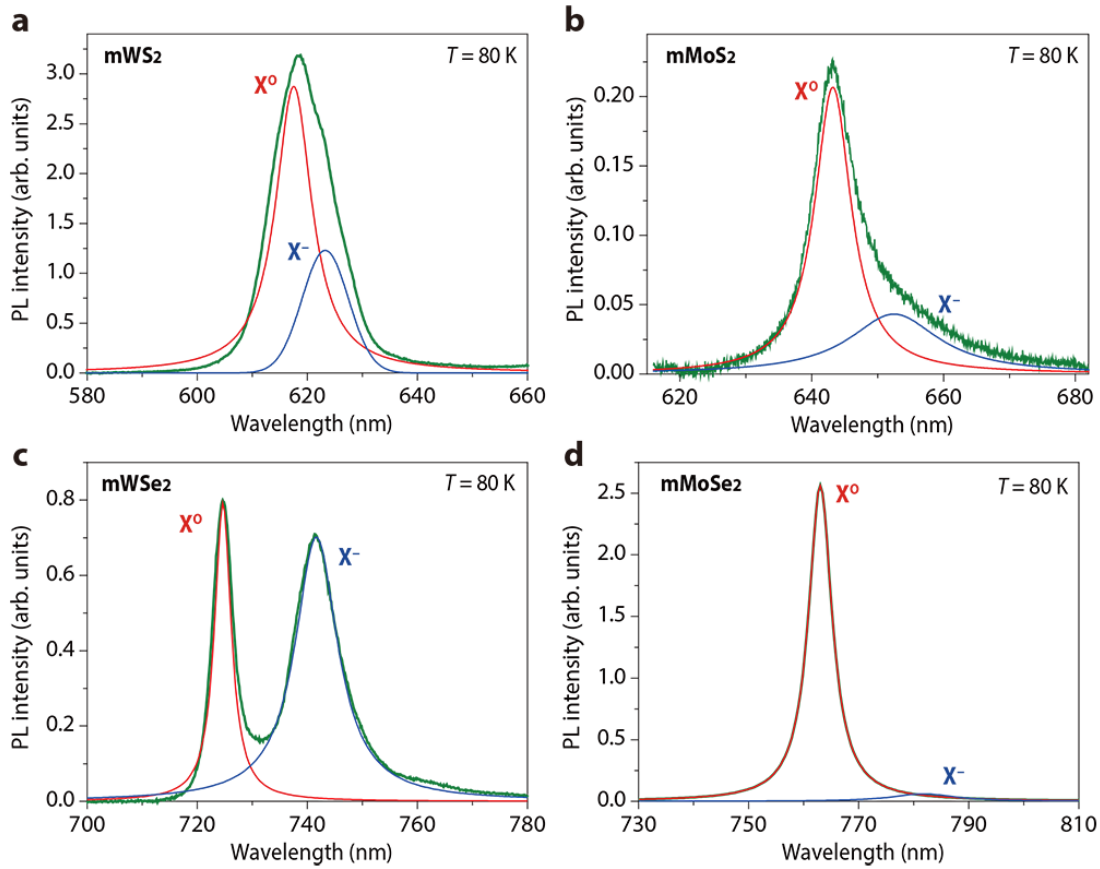
**Spectroscopic studies of atomic defects and bandgap renormalization in
semiconducting monolayer transition metal dichalcogenides**

Jeong et al.

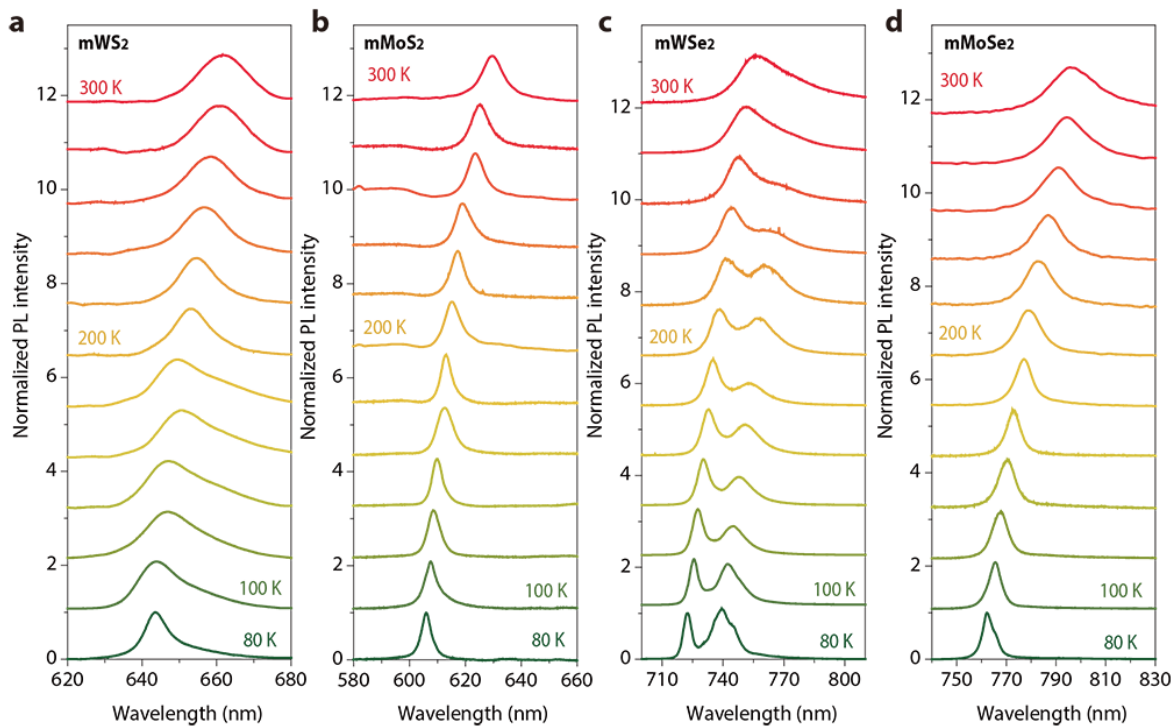
Supplementary Figures



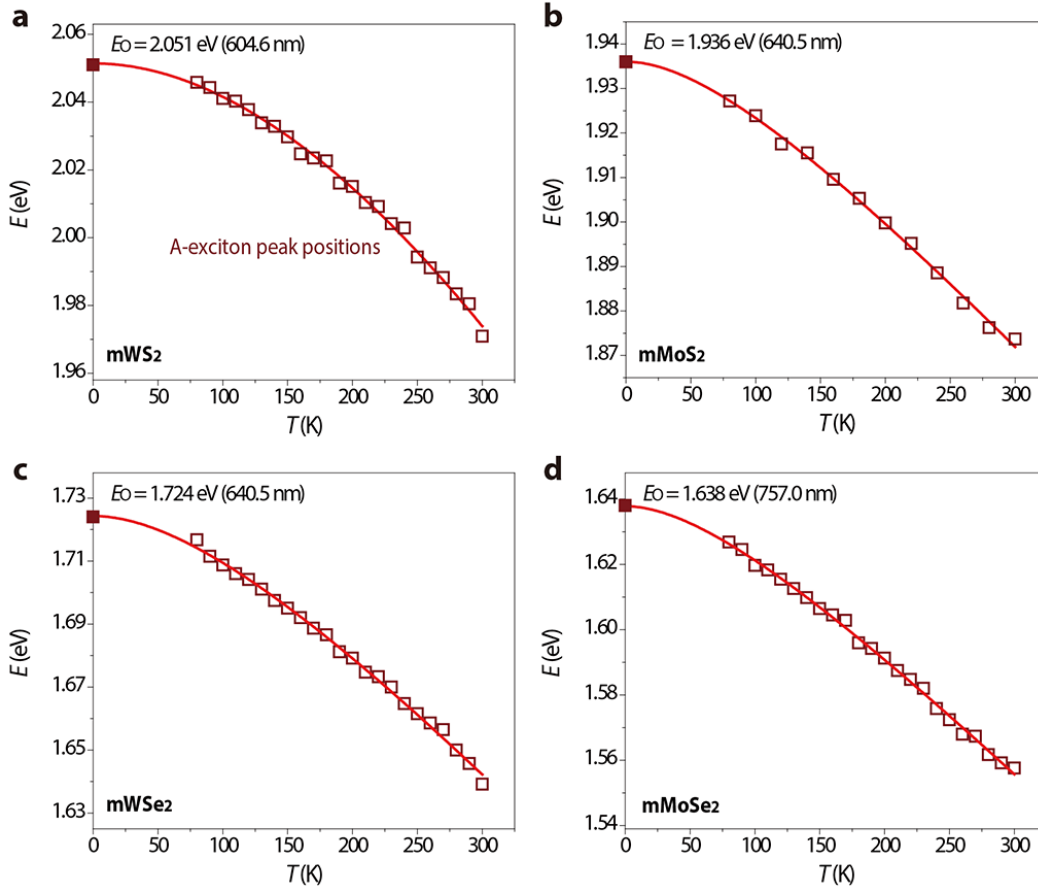
Supplementary Figure 1. Electron tunneling spectra of graphite–*h*-BN–graphene tunnel junctions. **a**, Series of dI/dV_b spectra from multiple planar tunnel junctions of single-layer graphene with graphite as a probe and thin *h*-BN as a tunnel barrier. Dirac points for all graphene tunnel junctions are close to the Fermi level ($V_b = 0$ mV) at $V_g = 0$ V. V_b is applied to the graphite probe and tunnel current is monitored through the graphene layer, in an identical setup as the measurements in the main text. Differences in dI/dV_b values are ascribed to tunnel *h*-BN layers and tunnel junction area. **b**, Scaled tunneling spectra adjusted with dI/dV_b multiplication constants to overlay with the dI/dV_b of device #05 (solid cyan line). Dotted green lines represent numerical fittings to the experimental data of device #05, requiring different fitting parameters for positive and negative V_b regions, which exhibit the electron–hole asymmetric electronic structures of the graphite–*h*-BN–graphene planar tunnel junctions. This fitting data, referred to as the graphene baseline, is used to analyze the electron tunneling spectra of the SC-mTMD-based planar junctions in the main text.



Supplementary Figure 2. Photoluminescence (PL) measurements of the SC-mTMD films. PL spectra displaying A-exciton peaks of the mWS₂ (a), mMoS₂ (b), mWSe₂ (c), and mMoSe₂ (d) films at $T = 80$ K. PL signals are collected right at the junction where the respective films are encapsulated by *h*-BN, graphite, and graphene layers in the planar tunnel junction platform. Pump light, CW Nd:YAG laser centered at 532 nm, is vertically shone onto the flakes through a $\times 50$ objective lens, and PL signals are collected through the same objective lens and analyzed with a liquid-nitrogen cooled Si CCD detector with 550 nm long pass filter. The positions of the A-exciton (X^0) peaks are determined by Lorentzian fittings with consideration of nearby charged excitons (X^-).



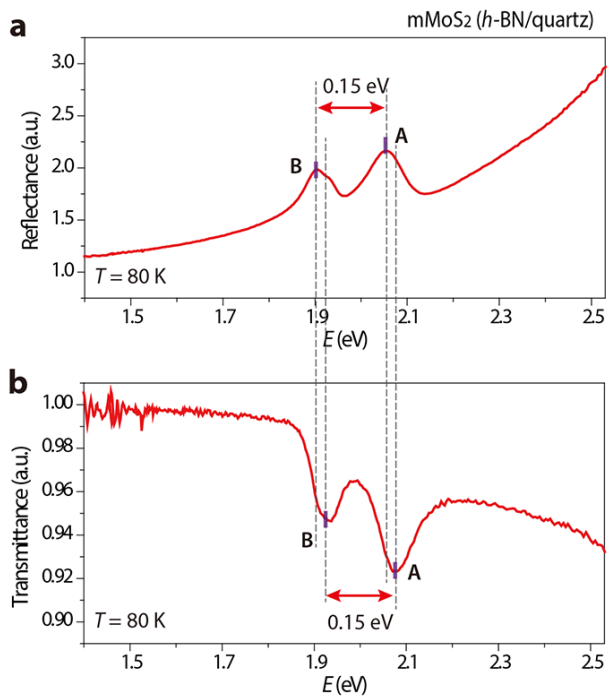
Supplementary Figure 3. Temperature-dependent PL measurements of the SC-mTMD films. Normalized PL spectra of mWS_2 (a), $mMoS_2$ (b), $mWSe_2$ (c), and $mMoSe_2$ (d) measured in the temperature range $80\text{ K} \leq T \leq 300\text{ K}$. Each spectrum is normalized to the maximum PL intensity. Moderate blue-shifts of the *A*-exciton peaks are universal in all four films.



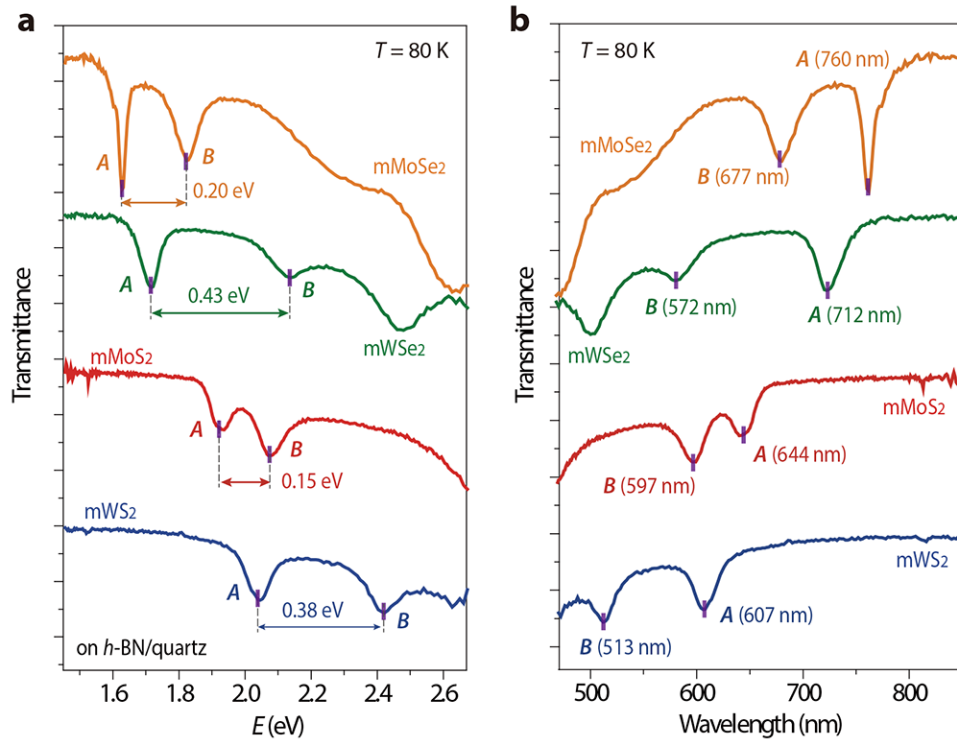
Supplementary Figure 4. Extracting the optical energy gaps of the SC-mTMD films. a–d Series of A-exciton peaks of the respective SC-mTMD films measured in the temperature range $80 \text{ K} \leq T \leq 300 \text{ K}$. Continuous blue-shift of the A-exciton peaks with decreasing temperature allows for the extraction of the intrinsic optical energy gaps of the films by following the peak positions to $T = 0 \text{ K}$, utilizing the Varshni relation that explains the temperature dependence of semiconductor energy gaps:

$$E_g(T) = E_o - \frac{\alpha T^2}{T + \beta},$$

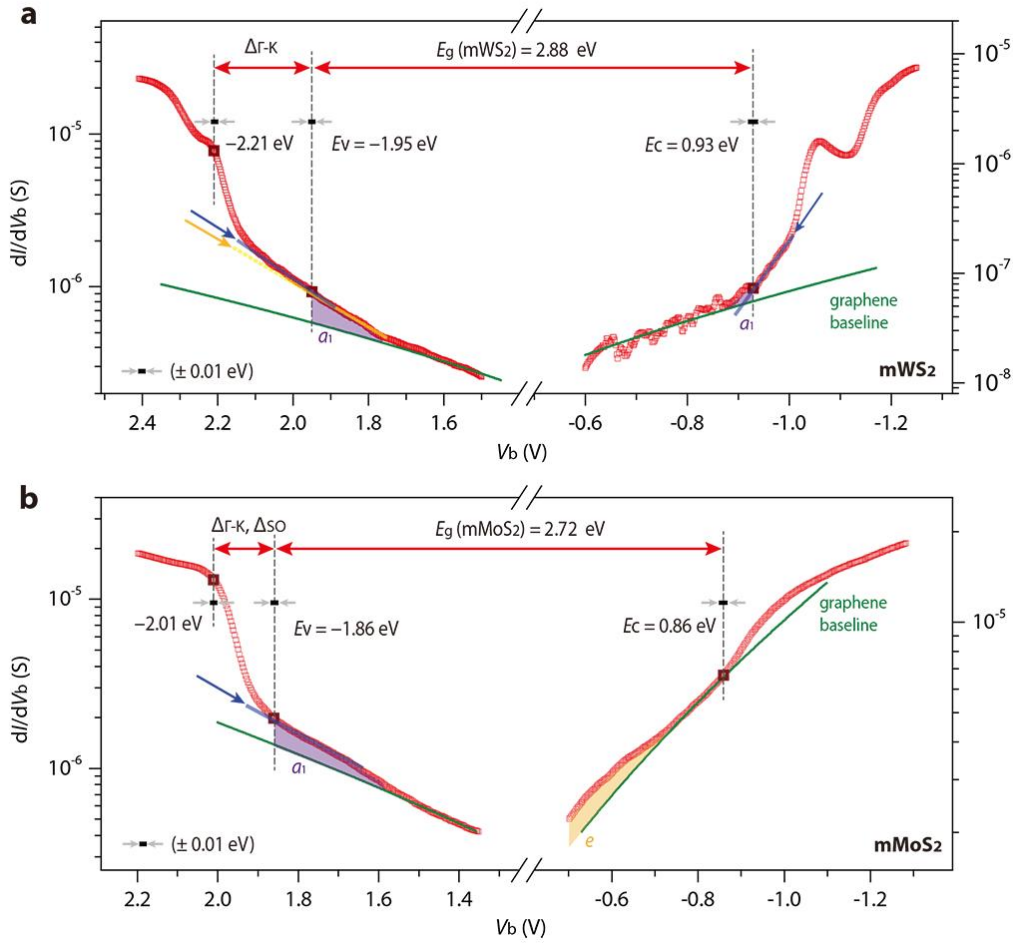
where E_o is the energy gap at $T = 0 \text{ K}$ and α and β are material-dependent fitting parameters.



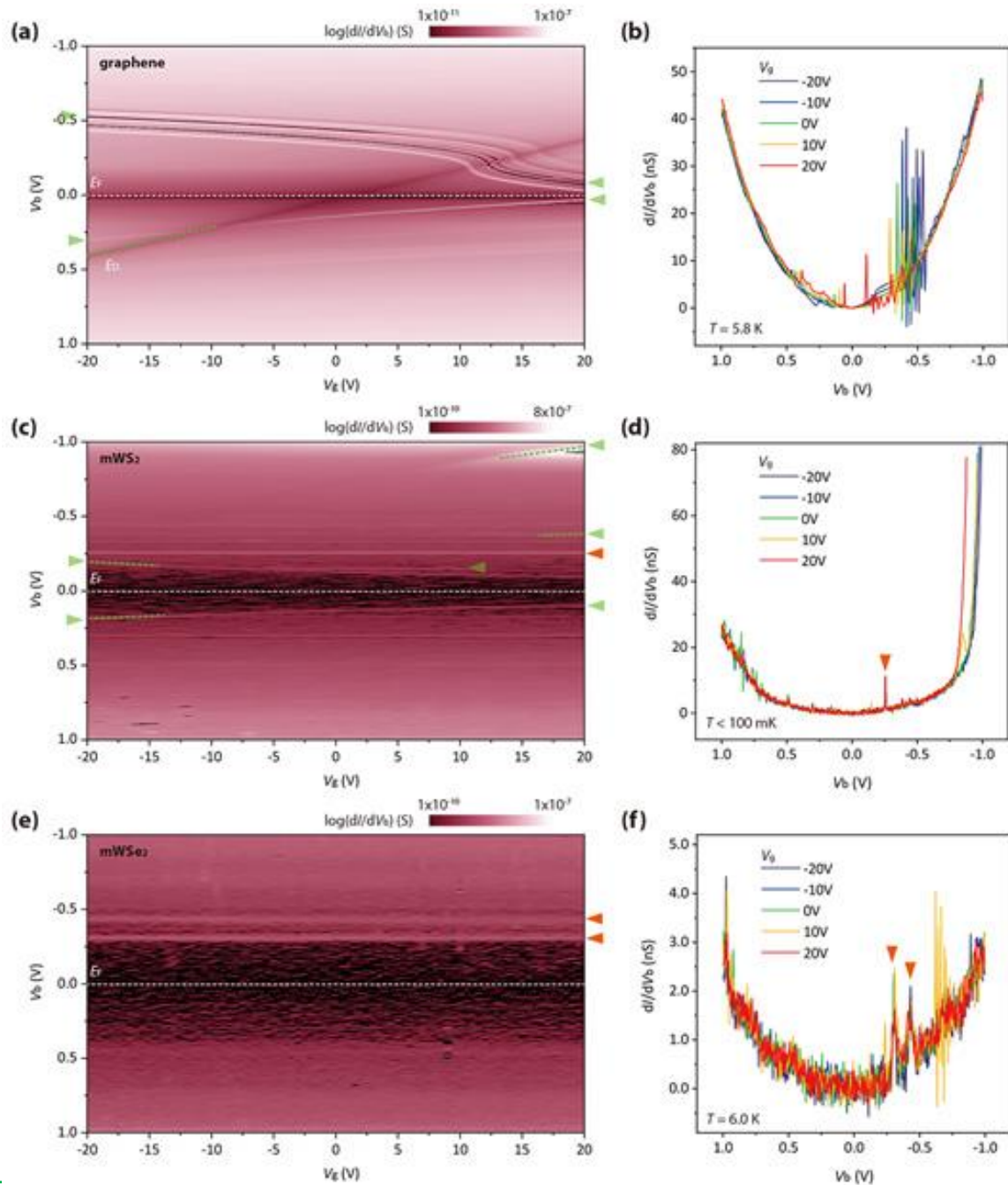
Supplementary Figure 5. Optical reflectance and transmittance measurements of mMoS₂. Optical reflectance (a) and transmittance (b) spectra of mMoS₂ film at $T = 80$ K. The film is transferred onto thick *h*-BN layers and then placed on a transparent quartz substrate. For reflectance and transmittance measurements, supercontinuum white source (NKT SuperK COMPACT supercontinuum lasers) is vertically shone onto the mMoS₂ film, mounted in a liquid nitrogen-cooled cryostat. Both optical measurements clearly show signals relating to the *A* and *B* excitons of the mMoS₂ film. The *A*–*B* exciton spacing, thereby spin-orbit coupling (SOC) induced valence band splitting of the mMoS₂, is estimated to be $\Delta_{SO}(\text{mMoS}_2) = 0.15 \pm 0.01$ eV. Note that individual exciton peak (a) and dip (b) positions in the reflectance and transmittance optical spectra are slightly off, attributed to different physical mechanisms in optical measurements.



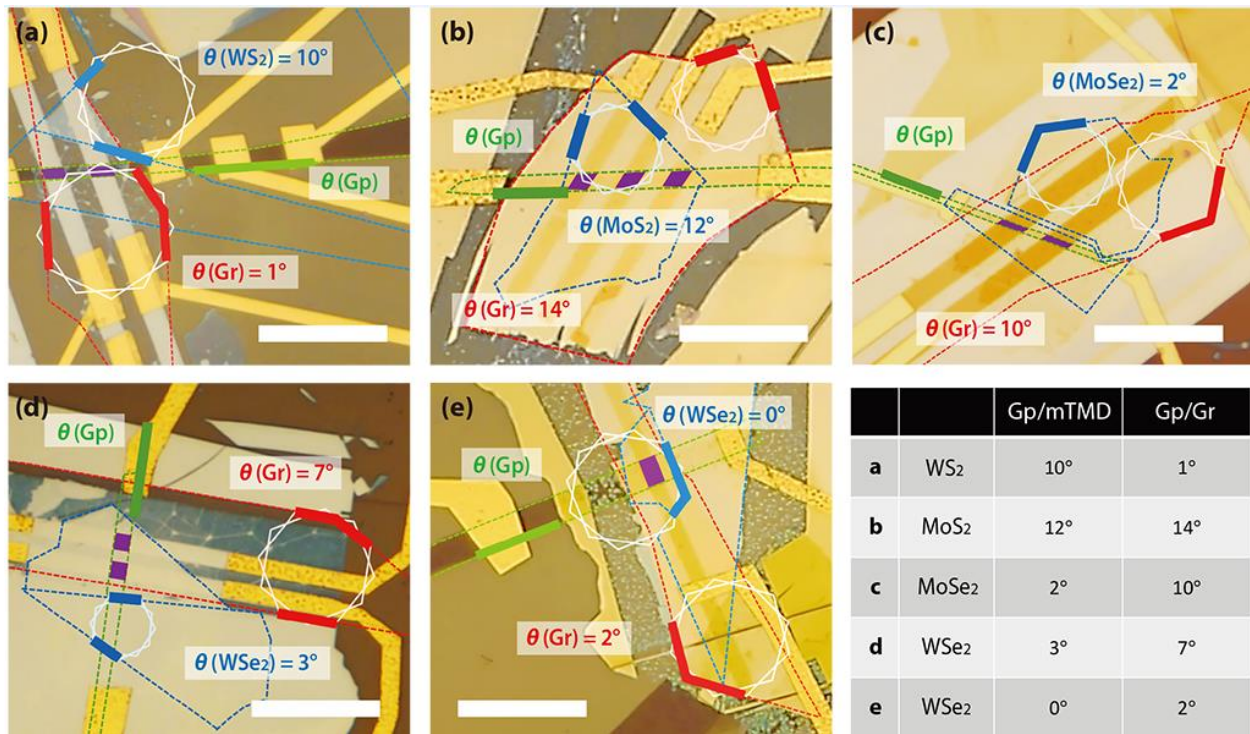
Supplementary Figure 6. A–B exciton spacing in SC-mTMD films. Series of optical transmittance spectra of the four respective films at $T = 80$ K, fabricated onto *h*-BN layers and a transparent quartz substrate at varying energy (a) and wavelength (b). The clearly resolved A–B excitonic peak spacings allow us to determine the SOC-induced valence-band splittings in all four films at high accuracy with an uncertainty level of less than ± 0.01 eV. Individual peak positions are extracted from numerical fittings to Lorentzian functions with baseline subtractions.



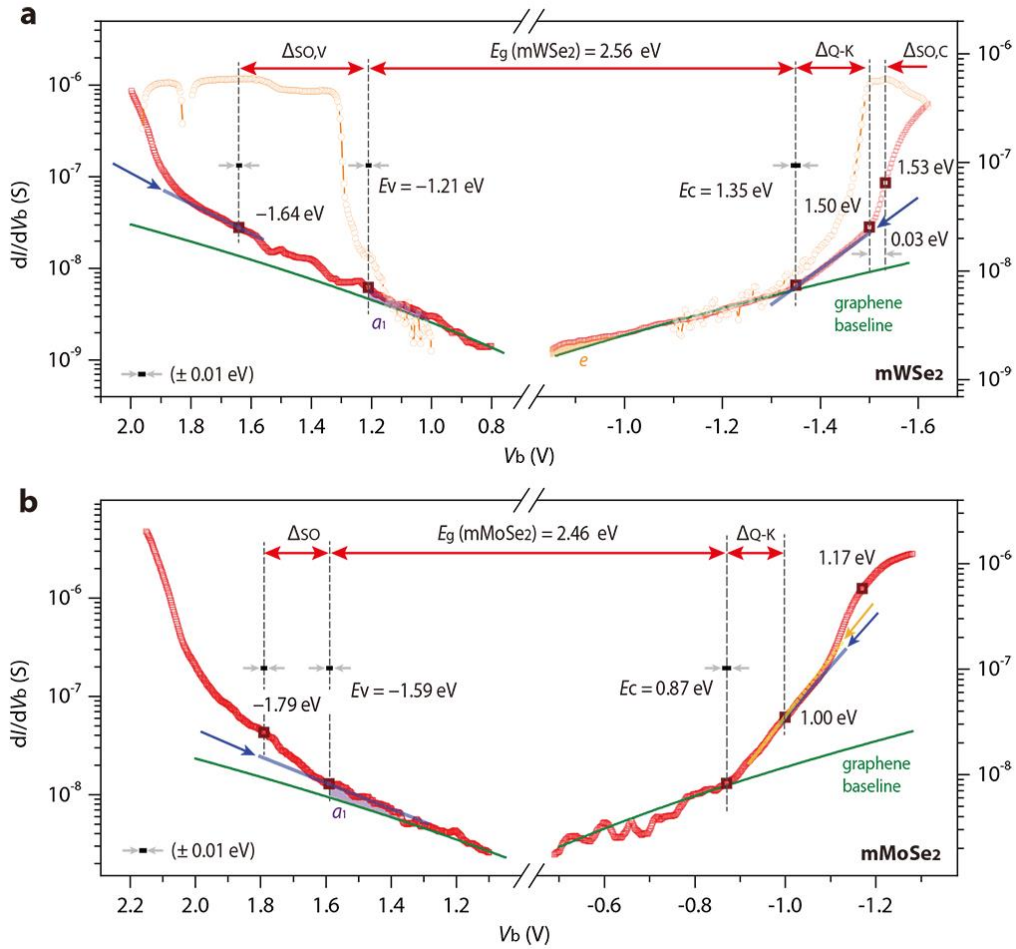
Supplementary Figure 7. Detailed electronic structure analyses of mWS₂ and mMoS₂ films. dI/dV_b tunneling spectra focused around the valence- and conduction-band edges of S-based mTMD films mWS₂ (a) and mMoS₂ (b). Valence band edges (the higher SOC-split band edge at the K point) are located based on the optically addressed *A–B* exciton spacings (Supplementary Figure 6) and eminent dI/dV_b features as marked with open brown squares. Conduction band edges are similarly located where the graphene baseline (green lines) and dI/dV_b spectra start deviating.



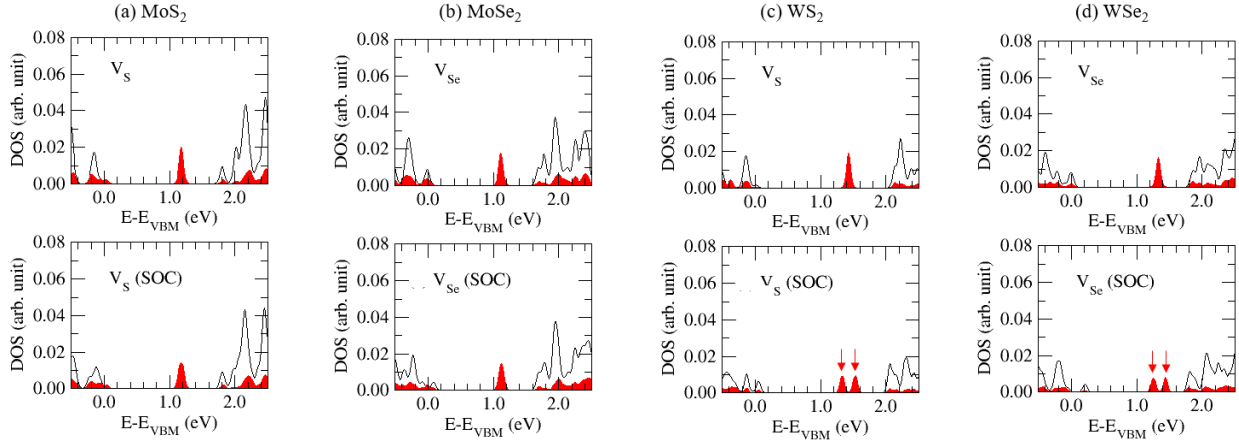
Supplementary Figure 8. Gate mappings and individual tunnel spectra for different tunnel junctions. Two-dimensional display of dI/dV_b curves at varying V_b and V_g for graphene (a), mWS₂ (c), mWSe₂ (e) based planar heterojunctions with a graphite as a tunnel probe and a thin *h*-BN as a tunnel insulator. The collections of individual dI/dV_b spectra at varying V_g are shown in (b) for the graphene, (d) for the mWS₂, and (f) for the mWSe₂ planar junctions.



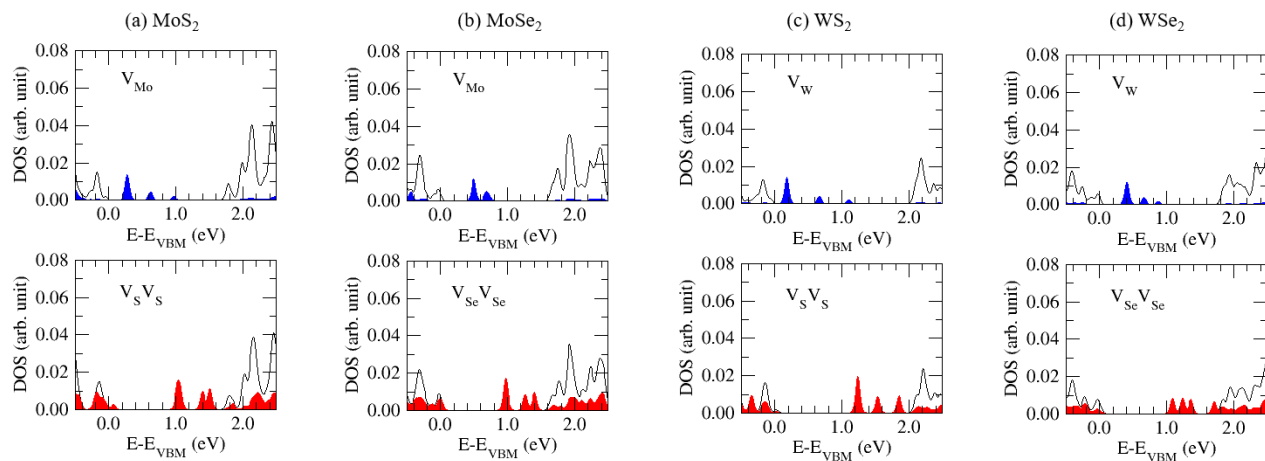
Supplementary Figure 9. Optical viewgraphs of SC-mTMD-based planar tunnel junctions. Optical images and the twist angle of SC-mTMD films and underlying graphene with respect to the top graphite for (a) mWS₂, (b) mMoS₂, (c) mMoSe₂, and mWSe₂ devices without (d) and with (e) angles aligned. Scale bars are 20 μm.



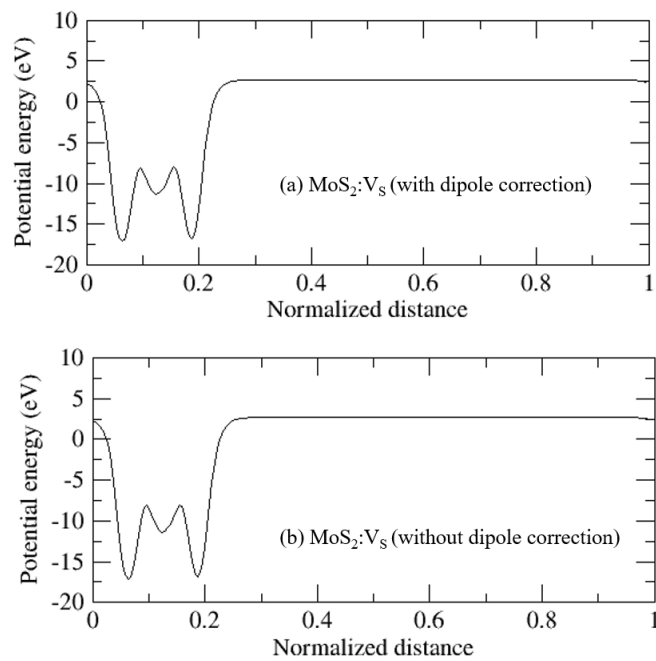
Supplementary Figure 10. Detailed electronic structure analyses of mWSe₂ and mMoSe₂ films. dI/dV_b tunneling spectra focused around the valence- and conduction-band edges of Se-based mTMD films mWSe₂ (**a**) and mMoSe₂ (**b**). Valence band edges and conduction band edges are found in the same manner as in Supplementary Figure 7.



Supplementary Figure 11. DFT results on single chalcogen-atom vacancies. **a–d**, Calculated defect density of states induced from single chalcogen-atom vacancies (V_S or V_{Se}) in four SC-mTMD films of **(a)** MoS₂, **(b)** MoSe₂, **(c)** WS₂, and **(d)** WSe₂ without (upper row) and with (lower row) consideration of SOC effects. The splits of the doublet e defect states in WS₂ and WSe₂ with the SOC are marked with red arrows.



Supplementary Figure 12. DFT results on single transition metal-atom and double chalcogen-atom vacancies. a–d, Calculated defect DOS for four SC-mTMD films of **(a)** MoS₂, **(b)** MoSe₂, **(c)** WS₂, and **(d)** WSe₂ from the missing of single transition-metal atoms (upper row, V_{Mo} or V_W) and double chalcogen-atom vacancies (lower row, V_SV_S or V_{Se}V_{Se}).



Supplementary Figure 13. DFT results on dipole correction. Plane-averaged local Hartree potentials for single sulfur vacancies in mMoS₂ films with (a) and without (b) dipole corrections.

Supplementary Table

			A (eV)	A (nm)	B (eV)	B (nm)	A-B (meV)
mMoSe₂	On quartz	80 K	1.632	759.6	1.841	673.7	209
	On quartz	300 K	1.574	787.8	1.773	699.3	199
	On <i>h</i> -BN	80 K	1.628	761.6	1.823	680.2	195
	Sandwiched	80 K	1.631	760.3	1.832	677.0	201
	Sandwiched	300 K	1.570	789.9	1.769	701.1	199
mWSe₂	On quartz	80 K	1.675	740.4	2.111	587.3	436
	On quartz	300 K	1.623	764.1	2.035	609.2	412
	On <i>h</i> -BN	80 K	1.712	724.2	2.128	582.7	416
	Sandwiched	80 K	1.742	712.0	2.169	571.8	427
	Sandwiched	300 K	1.681	737.8	2.094	592.2	413
mMoS₂	On <i>h</i> -BN	80 K	1.927	643.5	2.078	596.8	151
mWS₂	On <i>h</i> -BN	80 K	2.041	607.4	2.417	513.1	376

Supplementary Table 1. Exciton peaks of SC-mTMD films from optical transmittance measurements. *A*- and *B*-exciton peak positions of mMoSe₂, mWSe₂, mMoS₂, and mWS₂ from transmittance spectra in different dielectric environments: monolayer films on quartz substrates (on quartz), monolayers on *h*-BN and quartz (on *h*-BN), and encapsulated monolayers with *h*-BN flakes and placed on quartz substrate (sandwiched). Both *A*- and *B*-exciton peaks are more susceptible to nearby dielectric environments and temperature variations than the rather unresponsive *A*–*B* exciton spacings, whose values are estimated to be 200.6 ± 5.2 meV for mMoSe₂ and 420.8 ± 10.4 meV for mWSe₂ films. Uncertainty levels are further improved to 198.3 ± 3.1 meV for mMoSe₂ and 418.7 ± 7.4 meV for mWSe₂ when considering the case with high-quality non-interacting *h*-BN layers. We are thus able to assign with full confidence the SOC-induced valence band splittings of the four SC-mTMD films in the graphite–*h*-BN–graphene planar tunnel devices with an uncertainty level of ± 0.01 eV (Supplementary Figure 6), and later utilize them for analyzing the electronic structures of the semiconducting films with data from electron tunneling spectroscopy measurements.